



HAL
open science

Wind Instrument Sound Synthesis through Physical Modeling

Alexis Thibault

► **To cite this version:**

Alexis Thibault. Wind Instrument Sound Synthesis through Physical Modeling. Modeling and Simulation. 2019. hal-03230082v2

HAL Id: hal-03230082

<https://inria.hal.science/hal-03230082v2>

Submitted on 21 May 2021

HAL is a multi-disciplinary open access archive for the deposit and dissemination of scientific research documents, whether they are published or not. The documents may come from teaching and research institutions in France or abroad, or from public or private research centers.

L'archive ouverte pluridisciplinaire **HAL**, est destinée au dépôt et à la diffusion de documents scientifiques de niveau recherche, publiés ou non, émanant des établissements d'enseignement et de recherche français ou étrangers, des laboratoires publics ou privés.

Wind Instrument Sound Synthesis through Physical Modeling

Master's Thesis

M2 Mathématiques de la Modélisation

Alexis THIBAUT

Supervisor: Juliette Chabassier



Département de Mathématiques
et Applications
École Normale Supérieure
Paris



Département de Mathématiques
et Applications
Sorbonne Université
Paris

Inria

Équipe Magique3D
INRIA Bordeaux-Sud-Ouest

Motivations

The process of musical instrument design is traditionally based on lengthy experimentation on the part of instrument makers. Through repeated crafting and testing, they fine-tune the shapes and materials of their instruments in order to obtain the best results. This procedure is very time-consuming and expensive: indeed, numerous specific tools need to be manufactured, as well as many prototypes. However, combining the power of numerical systems with knowledge about musical acoustics may contribute to major evolutions in instrument-making.

At the Inria, team MAGIQUE-3D develops the OpenWIND toolbox¹, aimed at making state-of-the-art methods in musical acoustics accessible to all instrument makers. One of its already-available features was to compute the linear response of a wind instrument from its shape and physical characteristics. What it yet lacked was numerical synthesis of the *sound* of wind instruments, which would allow anyone to hear an instrument without having to manufacture it, and thus greatly easing the design process. Another use of this feature could be for historical and musicological purposes, to reconstruct the sound of instruments kept in museums that are too fragile to be played.

Sound synthesis is however a significant challenge, which requires time-domain solving of the equations of acoustic wave propagation in the instrument.

The aim of my internship was to understand the acoustical models for a wind instrument, adjust them for the time domain, and implement numerical schemes accordingly, in order to obtain physically accurate synthesized sounds. The main theoretical issues had to do with the presence of tone holes, sound radiation, reed embouchure, and viscothermal losses. For each of these, a well-behaved mathematical model must be found, before being able to write numerical schemes with the stability properties required for simulation.

Internship

This internship took place at the Inria Bordeaux–Sud-Ouest from April 23rd to August 30th, 2019. I worked closely with the section of the MAGIQUE-3D team in Bordeaux which focuses on musical acoustics, namely Juliette Chabassier (chargée de recherches Inria), Robin Tournemene (post-doc), Augustin Ernout (post-doc) and Guillaume Castera (master intern). The members of the team had very complementary fields of knowledge, which led to significant progress in the development of the OpenWIND toolbox.

After some time spent getting acquainted with basic musical acoustics, and with the mathematical theory of wave equations, I spent approximately six weeks studying the numerical schemes used for the pipes, junctions, radiation, and reed model. At the same time I was testing all these schemes, I kept thinking about an object-oriented structure for the code.

I began to write code for the toolbox at the beginning of June. I talked a lot with Robin, who authored most of the initial version of OpenWIND, about possible evolutions of the structure of the code, in order to make it as versatile as it would need to be (including frequency-domain but also time-domain

¹<https://openwind.gitlabpages.inria.fr/web/>

computations, and expandable to include the inverse problem of bore reconstruction), while keeping it tidy, organized and maintainable. The resulting ideas are explained briefly in chapter 3.

On July 2nd, the team met with Augustin Humeau, an instrument maker specialized in baroque bassoons and oboes. Augustin and Robin performed impedance measurements on a bassoon, while I presented the results of some recent sound simulations.

On July 9th, we presented our research to the rest of the MAGIQUE-3D team (based in Pau). Augustin talked about the issue of impedance measurement, and I about the numerical schemes presented here (with the exception of viscothermal effects).

The rest of my time was dedicated to the study of viscothermal losses, and to the improvement of the toolbox.

Seeing that the subject fascinated me, I chose to prolong my stay with a new internship starting in September, during my fourth year of schooling at ENS, with prospects of starting a Ph.D. thesis afterwards.

Contents

Motivations	1
Internship	1
Abstract	5
1 Acoustics of Wind Pipes	6
1.1 Lossless Pipes	6
1.1.1 Variational formulation	8
1.1.2 Conservation of energy	9
1.1.3 Space discretization	10
1.1.4 Time discretization	11
1.1.5 Energy conservation	13
1.1.6 CFL condition	13
1.2 Viscothermal Losses	14
1.2.1 The frequency-domain model	14
1.2.2 Fraction approximation	15
1.2.3 Time-domain system	19
1.2.4 Finite elements discretization in space	21
1.2.5 Time discretization	24
1.2.6 Energy balance	25
2 Around the Pipes	28
2.1 Boundary conditions	29
2.1.1 Flow condition	29
2.1.2 Pressure condition	29
2.1.3 Radiation impedance	30
2.1.4 Opening and closing holes	33
2.2 Junction of three pipes	33
2.2.1 Assembled version	34
2.2.2 Numerical scheme	35
2.2.3 Energy conservation	36
2.2.4 Schur complement	36
2.3 Reed model	36

3	Implementation	42
3.1	Sectioning of the toolbox	42
3.2	Scheme convergence	42
3.2.1	L^2 norm	43
3.2.2	Point-wise convergence	43
3.2.3	Radiation	43
3.2.4	Junction	43
3.2.5	Reed model	43
3.2.6	Viscothermal losses	44
3.2.7	A complex instrument: the bassoon	44
3.3	Energy conservation	44
3.3.1	Simple case: the cylindrical instrument	44
3.3.2	The bassoon	45
3.4	Sound synthesis	45
	Conclusion and perspectives	55

Abstract

In this report, we develop elementary numerical schemes to simulate time-domain evolution of individual parts of a wind instrument. A one-dimensional finite elements scheme for time-domain simulation of acoustic waves in a variable-section pipe is introduced, which includes viscothermal losses. Other schemes are presented for various boundary conditions, including acoustic radiation, as well as a pipe junction model useful for tone holes, and a reed model. These schemes are guaranteed to preserve energy, and can be assembled to form arbitrarily complex instruments with any number of tubes, holes, radiating parts and exciter mechanisms. Moreover, many parameters are permitted to vary continuously during the simulation without posing any stability concern. This allows to compute transient sounds from opening and closing of tone holes, or with varying reed parameters.

Chapter 1

Acoustics of Wind Pipes

A sustained-sound musical instrument involves the coupling of a resonator with a nonlinear mechanism. For bowed string instruments, the resonator is the string, and the nonlinearity comes from the interaction of the bow with the string. For wind instruments, the resonator is the air contained in the instrument itself, and the nonlinear source mechanism may be of various types, such as a single reed (clarinet, saxophone), a double reed (oboe, bassoon, duduk), the player's lips (trombone, didjeridoo), or a hydrodynamic jet (recorder, organ pipe, pan flute). With the player feeding energy into the system through the nonlinear mechanism, and the instrument reacting with a delay, a feedback loop is formed, which may result in a steady oscillation with a rich harmonic spectrum.

The differences in sounding frequency and timbre of instruments are in great part due to the resonator's response, that is, to the acoustic behavior of the instrument. To simulate a wind instrument, it is therefore necessary to accurately model the equations of acoustic waves.

In this chapter, we present a one-dimensional model for acoustic wave propagation in a variable-section pipe with no holes under plane wave hypothesis, and from it we derive a finite-element numerical scheme for time-domain simulation, using high-order finite elements. In the second section, the model is improved with viscous and thermal losses.

In chapter 2, we deal with the construction of a complete instrument from modular elements, with ideas similar to [40].

1.1 Lossless Pipes

The equations of acoustics stem from a simplification of the famous equations of Navier-Stokes, which describe well the motion of air:

$$\begin{cases} \partial_t \rho + \nabla \cdot (\rho v) = 0, \\ \partial_t (\rho v) + (v \cdot \nabla)(\rho v) + \nabla p - \nabla \cdot \tau = 0. \end{cases} \quad (1.1)$$

Here ρ is the air density, v the flow speed, p the pressure and τ is the viscous stress tensor. If we add the hypothesis that air is an ideal gas,

$$p = \rho RT \quad (1.2)$$

with specific heat at constant pressure C_P , and a formula for the viscous stress tensor, we could look for solutions of this problem. Its approximate numerical resolution is however very computer-intensive [43, 47]. A number of simplifying hypotheses can be made:

- Low flow speed: this allows to neglect convection term $(v \cdot \nabla)(\rho v)$.
- Low viscosity: this allows to neglect the viscous term $\nabla \cdot \tau$.
- Isentropic compression: this gives a direct proportionality between the rates of change of p and ρ .
- Small variation around atmospheric pressure and density: this allows to linearize the equations.

These simplifications, which are all standard assumptions in acoustics, lead to the linearized Euler equations. But in the specific case we are interested in, a further simplification can be done, to reduce the problem to only one dimension of space.

The instrument's bore may take various shapes : the clarinet, duduk and some organ pipes are mostly cylindrical, whereas the oboe, bassoon and saxophone are approximately conical, and the recorder and flute are slightly tapered. All these, however, exhibit a mostly linear shape (if we ignore the bends). We therefore simplify our model by supposing that the pipe is parametrized only by its cross-section $S(x)$, which varies slowly. Then, one can perform an asymptotic analysis to make the tube infinitely thin¹, which yields the following model [45]:

$$\begin{cases} \frac{\rho}{S} \partial_t v + \partial_x p = 0 & \text{on } \Omega, \\ \frac{S}{\rho c^2} \partial_t p + \partial_x v = 0 & \text{on } \Omega, \\ \text{B.C.}(p(\Omega_{(\pm)}), v(\Omega_{(\pm)}), \dots) & \text{on } \partial\Omega. \end{cases} \quad (1.3)$$

In the equations above, the unknowns are $p(x, t)$ and $v(x, t)$.

- $p(x, t)$ is the pressure at position x and time t .
- $v(x, t)$ is the instantaneous flow passing through $S(x)$ from left to right at time t .
- Parameter $\rho(x)$ is the average air density, around which the equations of acoustics are being linearized. It depends mainly on temperature, and may be space-dependent. Such a dependence can be useful to model non-uniform temperatures in the instrument due for example to the heat of the player's breath.
- Parameter $c(x)$ is the local celerity of acoustic waves, which mainly depends on air temperature.

We do not detail here the boundary conditions, which will be set to many different possibilities in chapter 2; but we need to keep in mind that they only

¹This is equivalent to making the assumption that surfaces of constant pressure are planar and orthogonal to the main axis.

constrain the values of p and v at the ends of pipes, with no regard for what happens away from the boundary.

Note that in the system of equations we consider, the air is bound to remain in the duct everywhere apart from the two ends. This model is therefore valid only for sections of tubing with no holes. In order to account for the presence of holes, we will join several pipes in T-shaped junctions. This will be done in section 2.2.

Because the influence of viscosity was neglected, viscous and thermal losses are not considered here. However, they play an important role in musical acoustics, as they are a key element of the perception of sound due to their major influence on the timbre [5]. Section 1.2 deals with these effects.

1.1.1 Variational formulation

Numerical solutions to problem (1.3) will be obtained through a finite-element discretization of the domain Ω [44]. To prepare for this Galerkin method, let us formulate the problem in variational form.

We look for unknowns $(p, v) \in H^1(\Omega) \times L^2(\Omega)^2$. Formally, we would like to have for all (\tilde{p}, \tilde{v}) in the same space:

$$\begin{cases} \int_{\Omega} \frac{\rho}{S} \partial_t v \tilde{v} + \int_{\Omega} \partial_x p \tilde{v} = 0 \\ \int_{\Omega} \frac{S}{\rho c^2} \partial_t p \tilde{p} + \int_{\Omega} \partial_x v \tilde{p} = 0. \end{cases}$$

However, as v should only belong to $L^2(\Omega)$, the factor $\partial_x v$ in the second formula does not make sense. Instead we must consider the formula after integration by parts.

$$\int_{\Omega} \frac{S}{\rho c^2} \partial_t p \tilde{p} - \int_{\Omega} \partial_x \tilde{p} v + (v(\Omega_{(-)}) \cdot n_{(-)}) \tilde{p}(\Omega_{(-)}) + (v(\Omega_{(+)}) \cdot n_{(+)}) \tilde{p}(\Omega_{(+)}) = 0,$$

where $n_{(\pm)}$ is the outwards-pointing unit vector. Here the terms $v(\Omega_{(\pm)}) \cdot n_{(\pm)}$ cannot correspond to pointwise evaluation of $v \in L^2(\Omega)$, so they must be replaced by additional variables $\lambda_{(-)}, \lambda_{(+)}$ describing these boundary values. We obtain the so-called *mixed variational formulation*:

$$\begin{cases} \int_{\Omega} \frac{\rho}{S} \partial_t v \tilde{v} + \int_{\Omega} \partial_x p \tilde{v} = 0 \quad \forall i = 1, 2, 3 \\ \int_{\Omega} \frac{S}{\rho c^2} \partial_t p \tilde{p} - \int_{\Omega} \partial_x \tilde{p} v + \lambda_{(-)} \tilde{p}(\Omega_{(-)}) + \lambda_{(+)} \tilde{p}(\Omega_{(+)}) = 0 \\ \text{B.C.}(p(\Omega_{(\pm)}), \lambda_{(\pm)}, \dots) \end{cases} \quad (1.4)$$

Finite element methods are usually expressed with bilinear and linear forms. Let us rewrite our problem in this framework. For any $v, \tilde{v} \in L^2(\Omega)$ and

²This choice of space is justified by its being well-suited for the Hille–Yosida theorem, which can be used to guarantee existence of solutions under some slack hypotheses on the boundary conditions. One proof of existence for a similar wave equation can be found in section 3.4.1 of [33].

$p, \tilde{p} \in H^1(\Omega)$, we denote :

$$m^{L^2}(v, \tilde{v}) := \int_{\Omega} \frac{\rho}{S} v \tilde{v} \quad (1.5)$$

$$m^{H^1}(p, \tilde{p}) := \int_{\Omega} \frac{S}{\rho c^2} p \tilde{p} \quad (1.6)$$

$$b(p, v) := - \int_{\Omega} v \partial_x p \quad (1.7)$$

$$e_{(\pm)}(p) := p(\Omega_{(\pm)}) \quad (1.8)$$

The system of equations is then written as :

$$\begin{cases} m^{L^2}(\partial_t v, \tilde{v}) - b(p, \tilde{v}) & = 0 \\ m^{H^1}(\partial_t p, \tilde{p}) + b(\tilde{p}, v) + \lambda_{(-)} e_{(-)}(\tilde{p}) + \lambda_{(+)} e_{(+)}(\tilde{p}) & = 0 \\ \text{B.C.}(e_{(\pm)}(p), \lambda_{(\pm)}, \dots) & \end{cases} \quad (1.9)$$

The boundary conditions now link the values of p at the extremities of the pipe with the unknown flows $\lambda_{(-)}$ and $\lambda_{(+)}$.

1.1.2 Conservation of energy

All throughout this report, we try to ensure the conservation or dissipation of some energy, which ensures good stability properties on the solution.

More specifically for the pipe, we are looking for an energy balance equation of the form

$$\frac{d}{dt} \mathcal{E}(p, v) = W(e_{(\pm)}(p), \lambda_{(\pm)}) - Q(p, v),$$

where $\mathcal{E} \geq 0$ is the energy of the pipe as a function of (p, v) , whereas $Q \geq 0$ is the dissipated power, and W is the external work on the pipe. Since viscothermal losses are neglected here, Q should be zero in the current case.

Setting $\tilde{v} = v$ and $\tilde{p} = p$ in (1.9) reveals the time derivative of $m^{L^2}(v, v)$ and of $m^{H^1}(p, p)$. We get the system of energies :

$$\begin{cases} \frac{1}{2} \frac{d}{dt} m^{L^2}(v, v) - b(p, v) = 0 \\ \frac{1}{2} \frac{d}{dt} m^{H^1}(p, p) + b(p, v) + \lambda_{(-)} e_{(-)}(p) + \lambda_{(+)} e_{(+)}(p) = 0 \end{cases} \quad (1.10)$$

The sum of these equations reads :

$$\frac{d}{dt} \mathcal{E} = -\lambda_{(-)} e_{(-)}(p) - \lambda_{(+)} e_{(+)}(p) \quad (1.11)$$

where the energy is defined as :

$$\mathcal{E} = \frac{1}{2} m^{L^2}(v, v) + \frac{1}{2} m^{H^1}(p, p). \quad (1.12)$$

Note that the convention here is that $\lambda_{(\pm)}$ is the outward-pointing part of v ; the same orientation convention must appear in the boundary conditions.

Under some assumptions on ρ , S and c , the quadratic forms associated to m^{L^2} and m^{H^1} are equivalent to the squared L^2 norm : indeed, if there exists constants C and C' such that :

$$\forall x \in \Omega, \begin{cases} 0 < C \leq \frac{\rho}{S}(x) \leq C' < +\infty \\ 0 < C \leq \frac{S}{\rho c^2}(x) \leq C' < +\infty, \end{cases} \quad (1.13)$$

then

$$\begin{aligned} \forall v \in L^2(\Omega), \quad & C^2 \|v\|_{L^2}^2 \leq m^{L^2}(v, v) \leq C'^2 \|v\|_{L^2}^2 \\ \forall p \in H^1(\Omega), \quad & C^2 \|p\|_{L^2}^2 \leq m^{H^1}(p, p) \leq C'^2 \|p\|_{L^2}^2. \end{aligned}$$

Therefore, any bounds on the energy yield similar bounds on the L^2 norm of the solution. In particular, if the boundary conditions are such that \mathcal{E} cannot exceed some maximal value, the L^2 -norms of p and v are bounded.

1.1.3 Space discretization

For space discretization we use a finite elements method, described in [11]. We replace spaces $H^1(\Omega)$ and $L^2(\Omega)$ with finite-dimensional spaces V_h and W_h , constructed with one-dimensional spectral finite elements [44]. That is, V_h and W_h are spanned by their respective bases $\{\phi_k\}$, $\{\psi_k\}$. Each of the basis functions is defined by parts, as Lagrange interpolation polynomials. The bilinear forms m^{L^2} , m^{H^1} and b are approximated using a quadrature procedure for mass lumping.

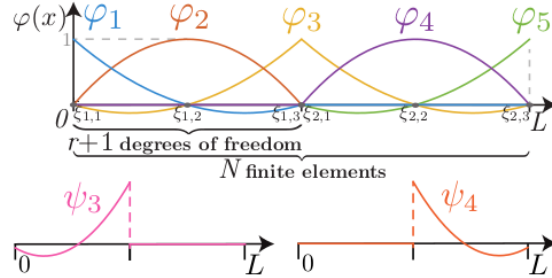


Figure 1.1: Basis functions used for finite elements, figure from [11]

All interpolation nodes and quadrature points are chosen to be Gauss-Lobato points. These choices allow us to use diagonal mass matrices, without any consistency loss:

$$M_{kl}^{L^2} := \int_{\Omega} \frac{\rho}{S} \psi_k \psi_l \quad (1.14)$$

$$M_{kl}^{H^1} := \int_{\Omega} \frac{S}{\rho c^2} \phi_k \phi_l \quad (1.15)$$

$$B_{kl} := - \int_{\Omega} \psi_k \partial_x \phi_l, \quad (1.16)$$

where \tilde{f} represents the approximate integral computed with a quadrature formula. We define the endpoint evaluation vectors:

$$E_{(\pm)} = (e_{(\pm)}(\phi_k))_k, \quad \text{i.e.} \quad E_{(-)} = \begin{pmatrix} 1 \\ 0 \\ \vdots \\ 0 \end{pmatrix}, \quad E_{(+)} = \begin{pmatrix} 0 \\ \vdots \\ 0 \\ 1 \end{pmatrix}$$

Vectors $E_{(\pm)}$ are used to evaluate the endpoints of $P \in V_h$: the associated linear forms are expressed as $e_{(\pm)}(P) = E_{(\pm)}^* P$. Given the space discretization we have chosen, the representation of $E_{(\pm)}$ on the (ϕ_k) basis contains a single 1 on the first (or last) degree of freedom of the segment Ω .

The space-discretized system of equations leads to the following semi-discrete problem: find $(P(t), V(t), \lambda_{(\pm)}(t))$ in $V_h \times W_h \times \mathbb{R}^2$, such that for all times $t \in [0, T]$:

$$\begin{cases} M^{L^2} \partial_t V - BP = 0 \\ M^{H^1} \partial_t P + B^* V + \lambda_{(-)} E_{(-)} + \lambda_{(+)} E_{(+)} = 0, \\ \text{B.C. } (E_{(\pm)}^* P, \lambda_{(\pm)}, \dots) \end{cases} \quad (1.17)$$

The same energy equation as before remains valid, but it is now expressed with finite-dimensional operators.

$$\mathcal{E} = \frac{1}{2}(V^* M^{L^2} V) + \frac{1}{2}(P^* M^{H^1} P), \quad (1.18)$$

$$\frac{d}{dt} \mathcal{E} = -\lambda_{(-)} E_{(-)}^* P - \lambda_{(+)} E_{(+)}^* P. \quad (1.19)$$

Now we must find a time-discrete scheme in order to compute an approximate solution.

1.1.4 Time discretization

We choose to perform a leap-frog integration on the (P, V) variables. The evaluation times of P and V are staggered, so that given some time step $\Delta t > 0$, we approximate $P(n\Delta t) \approx P^n$ and $V((n + \frac{1}{2})\Delta t) \approx V^{n+1/2}$.

Discrete-time operators

Before writing the scheme, we define discrete differentiation operator δ , and averaging operator μ , as:

$$\delta V^n = \frac{V^{n+1/2} - V^{n-1/2}}{\Delta t}, \quad \mu V^n = \frac{V^{n+1/2} + V^{n-1/2}}{2}. \quad (1.20)$$

Note how δV and μV are then defined on integer values, where V had time superscripts of the form $n + 1/2$. Conversely, P takes integer superscripts, but δP and μP are defined on the staggered grid. One can see δ and μ as time-domain convolution operators. Also note that it is possible to apply them several times: for instance $\mu\mu P^n = 1/4(P^{n-1} + 2P^n + P^{n+1})$. It is easy to notice that they commute: $\delta\mu = \mu\delta$.

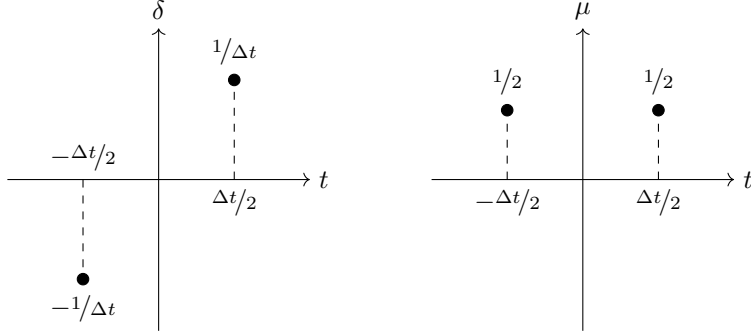


Figure 1.2: Operators δ and μ correspond to a time-domain convolution of the discrete data.

Inner products with δ and μ

Some properties regarding the interaction of operators δ and μ with inner products will be necessary in order to find a discrete energy balance.

Let $\langle \cdot, \cdot \rangle$ denote an inner product on a vector space E , with corresponding norm $\|f\|^2 = \langle f, f \rangle$. Let $(f^{n+1/2})_{n=0,1,\dots}$ be a sequence of elements of E . We define $N(f)^n := \langle f^{n+1/2}, f^{n-1/2} \rangle$ the “mid-time norm” of f (which is not actually a norm, because it may be negative). Then one has the following equalities:

$$\delta \left(\frac{1}{2} \|f\|^2 \right) = \langle \mu f, \delta f \rangle, \quad (1.21)$$

$$\delta \left(\frac{1}{2} N(f) \right) = \langle f, \mu \delta f \rangle, \quad (1.22)$$

$$N(f) = \|\mu f\|^2 - \frac{\Delta t^2}{4} \|\delta f\|^2, \quad (1.23)$$

$$N(f) = \mu \|f\|^2 - \frac{\Delta t^2}{2} \|\delta f\|^2, \quad (1.24)$$

$$\langle f, \mu \mu f \rangle = \mu \|\mu f\|^2 - \frac{\Delta t^2}{8} \delta \delta \|f\|^2. \quad (1.25)$$

These properties will be used to obtain quadratic forms for energy balance, both in this section, and in the section about viscothermal losses.

The scheme

Our time-discrete numerical scheme is:

$$\begin{cases} \text{B.C.}^{n+1/2} \left(E_{(\pm)}^* \mu P^{n+1/2}, \lambda_{(\pm)}^{n+1/2}, \dots \right), \\ M^{H^1} \delta P^{n+1/2} + B^* V^{n+1/2} + \lambda_{(-)}^{n+1/2} E_{(-)} + \lambda_{(+)}^{n+1/2} E_{(+)} = 0, \\ M^{L^2} \delta V^{n+1} - B P^{n+1} = 0 \end{cases} \quad (1.26)$$

As the boundary conditions have not yet been expressed, it is not obvious to see why this scheme is explicit (or implicit only at boundary points). We will see that $\lambda_{(\pm)}^{n+1/2}$ are easy to compute in the useful case of linear (or well-behaved

nonlinear) boundary conditions, and do not require sub-iterations. Once they are known, it is possible to deduce P^{n+1} , and subsequently $V^{n+3/2}$, etc.

1.1.5 Energy conservation

Let us show that iterates of this scheme verify an energy balance equation similar to (1.19). Taking the half-sum of the equation on V at time steps n and $n+1$, and multiplying the equation on P by the appropriate factor $\mu P^{n+1/2}$ yields:

$$\begin{cases} (V^{n+1/2})^* M^{L^2} \mu \delta V^{n+1/2} - (V^{n+1/2})^* B \mu P^{n+1/2} = 0 \\ (\mu P^{n+1/2})^* \left(M^{H^1} \delta P^{n+1/2} + B^* V^{n+1/2} + \lambda_{(-)}^{n+1/2} E_{(-)} + \lambda_{(+)}^{n+1/2} E_{(+)} \right) = 0, \end{cases} \quad (1.27)$$

The sum of these equations results in a first discrete energy conservation equation:

$$\mathcal{E}^n = \frac{1}{2} (V^{n+1/2})^* M^{L^2} V^{n-1/2} + \frac{1}{2} (P^n)^* M^{H^1} P^n \quad (1.28)$$

$$\frac{\mathcal{E}^{n+1} - \mathcal{E}^n}{\Delta t} = -\lambda_{(-)}^{n+1/2} E_{(-)}^* \mu P^{n+1/2} - \lambda_{(+)}^{n+1/2} E_{(+)}^* \mu P^{n+1/2} \quad (1.29)$$

Note the similarity with (1.19). Also note that the first term of this energy compares V at two different times $n-1/2$ and $n+1/2$, so it corresponds to $N(V)^n$, with N being the ‘‘mid-time norm’’ from before, for the scalar product associated with M^{L^2} .

1.1.6 CFL condition

The problem with energy (1.28) is that the first term may be negative in case of fast oscillations, resulting in an unstable scheme. We must ensure that the energy remains a positive quadratic form. Let us rewrite it in terms of μV^n and P^n :

$$\begin{aligned} (V^{n+1/2})^* M^{L^2} V^{n-1/2} &= \left(\mu V^n - \frac{\Delta t}{2} B P^n \right)^* M^{L^2} \left(\mu V^n + \frac{\Delta t}{2} B P^n \right) \\ &= (\mu V^n)^* M^{L^2} \mu V^n - \frac{\Delta t^2}{4} (B P^n)^* M^{L^2} (B P^n) \end{aligned}$$

Therefore the energy can also be written as:

$$\mathcal{E}^n = \frac{1}{2} (\mu V^n)^* M^{L^2} \mu V^n + \frac{1}{2} (P^n)^* M_{\Delta t}^{H^1} P^n, \quad (1.30)$$

where $M_{\Delta t}^{H^1}$ is a modified mass matrix:

$$M_{\Delta t}^{H^1} = M^{H^1} - \frac{\Delta t^2}{4} B^* M^{L^2} B. \quad (1.31)$$

The energy (1.30) is positive definite if and only if $M_{\Delta t}^{H^1}$ is. A sufficient condition to ensure positivity is:

$$\Delta t < 2 \left[\rho \left((M^{H^1})^{-1} B^* M^{L^2} B \right) \right]^{-\frac{1}{2}}, \quad (1.32)$$

where $\rho(M)$ denotes the spectral radius of matrix M . This is our stability condition.

Remark. *The stability condition only depends on the meshing. It is a complicated problem to find a mesh that gives good precision while maintaining a small spectral radius. The main advantage of Finite Element Methods is that it is possible to increase the order of the elements individually, leading to an excellent rate of convergence for space discretization, while keeping the computational cost under control. The choice of the discretization in itself is a research topic [2,42], which I did not focus on. Robin Tournemenne and Guillaume Castera worked on those aspects more specifically in the context of OpenWIND.*

Remark. *The stability condition of the whole instrument will correspond to the most restrictive of the different elements' stability conditions. In case the pipe corresponds to a short tone hole, it may be useful to make the discretization of the hole relatively rough (single element, and low order). Otherwise the CFL condition of the hole may easily be more limiting than that of the main pipe, and so the time step Δt would be limited by the tone hole discretization. One possible idea to overcome this issue would be to implement locally implicit schemes on small pipes [18,41].*

1.2 Viscothermal Losses

Energy dissipation phenomena are of principal importance in instrument modeling, due to their significant effect on the resonant frequencies and perceived timbre of musical instruments [37]. In particular, viscothermal losses, which occur on the boundary layer of the instrument's bore due to friction of air against the duct, must be accounted for in order to obtain meaningful results [36]. They pose an especially challenging problem, because the acoustical model cannot be easily converted to time-domain equations.

1.2.1 The frequency-domain model

As before, we consider an axisymmetric tube with variable section $S(x) = \pi R(x)^2$. One possible model [12] for wave propagation in the tube which takes into account viscothermal losses is:

$$\frac{d\hat{p}}{dx} + Z\hat{v} = 0 \quad \text{and} \quad \frac{d\hat{v}}{dx} + Y\hat{p} = 0, \quad (1.33)$$

where \hat{p} and \hat{v} denote the pressure and flow in harmonic regime (i.e. as functions of space and frequency, instead of space and time). Immitances Z and Y take the following form:

$$Z = \frac{\rho}{S} j\omega \frac{1}{1 - F_v}, \quad (1.34)$$

$$Y = \frac{S}{\rho c^2} j\omega [1 + (\gamma - 1)F_\theta]. \quad (1.35)$$

Here ρ is air density, γ is the ideal gas constant, and c is the velocity of the wave. Coefficients F_v and F_θ describe the contribution of respectively viscous

and thermal dissipation, and are given by:

$$F_v(\omega) = \phi \left(R \sqrt{-\frac{j\omega}{cl_v}} \right), \quad (1.36)$$

$$F_\theta(\omega) = \phi \left(R \sqrt{-\frac{j\omega}{cl_\theta}} \right), \quad (1.37)$$

$$\text{with } \phi(\alpha) = \frac{2J_1(\alpha)}{\alpha J_0(\alpha)}. \quad (1.38)$$

Here J_0 and J_1 are zeroth- and first-order Bessel functions, and l_v and l_θ are characteristic lengths of viscous effects and thermal diffusion, given by $l_v = \frac{\mu}{\rho c}$ and $l_\theta = \frac{\kappa}{\rho c C_P}$ [12]. Note that Bessel functions are even, so that there is no issue with the complex square root.

Following the work by Bilbao [8], we split the immittances into conservative and non-conservative parts:

$$Z = Z_l + Z_v, \quad \text{and} \quad Y = Y_l + Y_\theta, \quad (1.39)$$

where $Z_l = \frac{\rho}{S} j\omega$ and $Y_l = \frac{S}{\rho c^2} j\omega$ correspond to lossless wave propagation. Neglecting Z_v and Y_θ , one would recover Webster's horn equation [45]. The contributions of viscothermal losses to the immittances are:

$$Z_v = \frac{\rho}{S} \frac{j\omega F_v}{1 - F_v}, \quad (1.40)$$

$$Y_\theta = \frac{S}{\rho c^2} (\gamma - 1) j\omega F_\theta. \quad (1.41)$$

Finding a partial differential equation in time with the correct behavior is problematic, because of the complicated form of Z_v and Y_θ .

1.2.2 Fraction approximation

In order to arrive at an explicit time-domain model, immittances Z_v and Y_θ need to be approximated. One possible method is to write them as a partial fraction decomposition, more specifically by a sum of first-order high-pass filters. This approximation is well-suited for the time domain, but it has been shown to converge very slowly [9].

Methods have been devised where the coefficients to these filters are optimized for each possible radius [8].

We present an approximation method where coefficients can be optimized once and for all without any knowledge on the geometry of the pipe. Such a result will allow us to write equations with explicit values for the coefficients.

We introduce characteristic times:

$$\tau_v(x) := \frac{R(x)^2}{cl_v}, \quad \tau_\theta(x) := \frac{R(x)^2}{cl_\theta}, \quad (1.42)$$

and a dimensionless function $G(\zeta)$, which describes the amount of losses, depending on a dimensionless variable ζ :

$$G(\zeta) = \frac{j\zeta \phi(\sqrt{-j\zeta})}{1 - \phi(\sqrt{-j\zeta})}, \quad (1.43)$$

so that Z_v can be rewritten as

$$Z_v = \frac{\rho}{S} \frac{1}{\tau_v} G(\zeta_v), \quad \text{where } \zeta_v := \tau_v \omega. \quad (1.44)$$

Nondimensionalized frequency ζ_v describes the regime of viscous losses at a given frequency, taking into account the pipe's radius and ambient physics. Its range of interest for applications in musical acoustics lies approximately between 1 and 1×10^8 , but may extend lower for very thin pipes.

- When ζ_v is low (less than about 10), function $G(\zeta_v)$ is almost constant, with a limit equal to 8 as $\zeta \rightarrow 0$.
- When ζ_v is large, $G(\zeta_v)$ is asymptotically equivalent to $\sqrt{2\zeta_v}$. This high-frequency behavior is thus well-approximated by fractional derivatives, the time-domain computation of which remains a topic of research [25].

As proposed in [8], we also split Y_θ into:

$$Y_\theta = \frac{S}{\rho c^2} \frac{1}{\frac{1}{\gamma-1} + \frac{1}{\tilde{Y}_\theta}}, \quad (1.45)$$

where \tilde{Y}_θ is of the same form as Z_v :

$$\tilde{Y}_\theta = (\gamma - 1) \frac{1}{\tau_\theta} G(\zeta_\theta), \quad \text{with } \zeta_\theta = \tau_\theta \omega. \quad (1.46)$$

This unified form is useful because it makes it possible to approximate only function G , rather than finding different forms for Y_θ and Z_v .

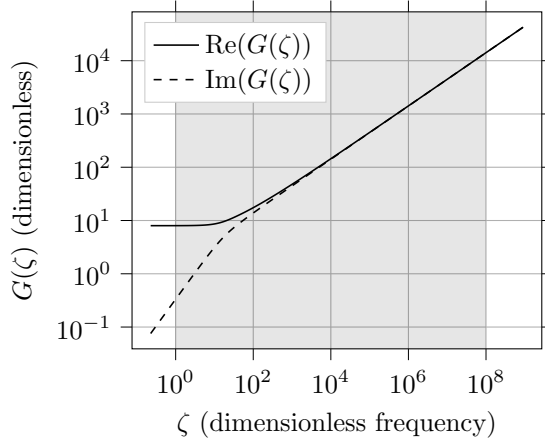


Figure 1.3: Dimensionless function G , as a function of regime variable $\zeta = \frac{R^2 \omega}{c \ell_{v,\theta}}$. The range of interest of nondimensionalized frequency ζ for applications in musical acoustics lies approximately between 1 and 1×10^8 (grayed zone). Note the low-frequency limit $G(0) = 8$, and the high-frequency behavior $G \sim \sqrt{2\zeta}$.

We choose to approximate G by functions G^N of the following form:

$$G^N(\zeta) = a_0 + \sum_{i=1}^N \frac{a_i j \zeta}{b_i j \zeta + 1}, \quad (1.47)$$

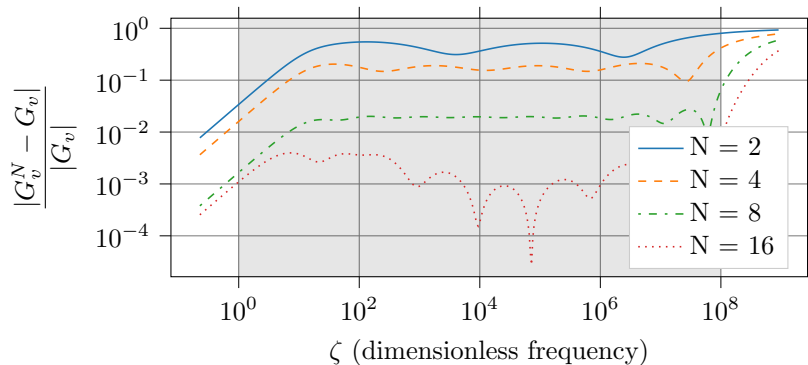


Figure 1.4: Fractional error on the approximation of G by G^N , as a function of dimensionless variable ζ . Optimization is performed for ζ ranging between 1 and 1×10^8 . The approximation is very good in the low-frequency range due to the constant term a_0 .

where $(a_i, b_i)_{i=1\dots N}$ are chosen with an optimization procedure, and $a_0 = 8$ in order to fit the low-frequency behavior. All these values must be positive, to ensure passivity.

The choice of this form is motivated by two main reasons:

- Noting that function G has only negative real roots in the Laplace domain suggests to use a partial fraction decomposition, inspired by the signal processing community [9].
- The similarity of high-frequency behavior with a fractional derivative operator hints at using a number of dampers, a technique used for instance in [6]. It is interesting to note that fractional derivatives can be exactly represented in this way, though by a continuum of high-pass filters [25,27]:

$$(j\omega)^\alpha = \int_{\xi \in \mathbb{R}^+} \frac{\mu_{1-\alpha}(\xi) j\omega}{\xi j\omega + 1} d\xi, \quad (1.48)$$

where $\mu_{1-\alpha}(\xi) = \frac{\sin(\alpha\pi)}{\pi} \xi^{\alpha-1}$. This *diffusive representation* allows to express theoretical results of existence of strong solutions to the Webster-Lokshin model with fractional derivatives³ [24]. From equation (1.48) can also be deduced reasonable initial values for the coefficients of G^N prior to optimization.

In contrast to what is used in [8,46], given a number of oscillators N , a single optimization must be performed to approximate G once and for all, rather than one optimization for every possible radius. The objective function is chosen to be

$$E = \sum_{k=1}^M \frac{|G^N(\zeta_k) - G(\zeta_k)|}{|G(\zeta_k)|}, \quad (1.49)$$

where ζ_k are $M = 100$ exponentially spaced values, spanning the range of interest. In table 1.1 we give values of coefficients (a_i, b_i) optimized to minimize this

³A similar strong existence result could be proved on our initial model (1.33) provided a diffusive representation of G is found.

sampled L^2 error. Figure 1.4 represents the fractional error on G as a function of the frequency, for several values of N . As the range of interest of ζ is very large (about 8 orders of magnitude), more oscillators are necessary compared to cases with a smaller range of frequencies [6].

Replacing G with G^N yields approximations of immittances Z_v and \tilde{Y}_θ :

$$Z_v^N = \frac{\rho}{S} \left[\frac{a_0}{\tau_v} + \sum_{i=1}^N \frac{a_i j\omega}{b_i \tau_v j\omega + 1} \right] \quad (1.50)$$

$$\tilde{Y}_\theta^N = \frac{\gamma - 1}{\tau_\theta} a_0 + \sum_{i=1}^N \frac{(\gamma - 1) a_i j\omega}{b_i \tau_\theta j\omega + 1}. \quad (1.51)$$

These equations can be represented as an equivalent electronic circuit with Foster structure, similar to [8] (see figure 1.5)⁴. This form of immittances is convenient because each corresponds to a system of ordinary differential equations in the time domain, with local additional variables.

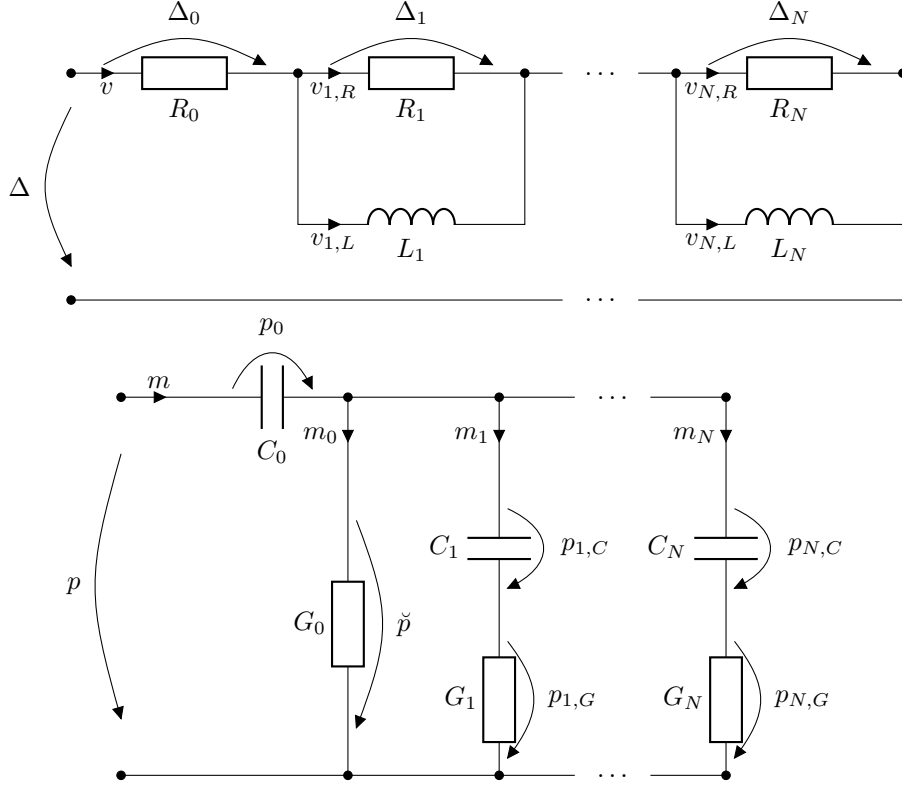


Figure 1.5: Electronic circuit representation of system 1.53 as Foster structures. For ease of notation, R_0 and R_i denote resistance values whereas G_0 and G_i are conductances, L_i are inductances, and C_0 and C_i are capacitances.

⁴With this convention, Z_v^N corresponds to the harmonic-domain ratio $\frac{\hat{\Delta}}{\hat{v}}$, and Y_θ^N to the ratio $\frac{\hat{m}}{\hat{p}}$.

1.2.3 Time-domain system

Replacing the approximated immitances $Z^N = Z_l + Z_v^N$ and $Y^N = Y_l + Y_\theta^N$ in equation (1.33), the diffusive representations can be exploited to translate the frequency-domain system to the time domain. We obtain:

$$\begin{cases} \partial_x p + \frac{\rho}{S} \partial_t v + \Delta = 0, \\ \partial_x v + \frac{S}{\rho c^2} \partial_t p + m = 0, \end{cases} \quad (1.52)$$

where Δ and m are correction terms corresponding to viscous and thermal losses respectively. They are expressed as:

$$\Delta = \Delta_0 + \sum_{i=1}^N \Delta_i, \quad m = m_0 + \sum_{i=1}^N m_i, \quad (1.53)$$

$$\Delta_0 = R_0 v, \quad m_0 = G_0 \check{p}, \quad (1.54)$$

$$\Delta_i = R_i v_{i,R} = L_i \frac{dv_{i,L}}{dt}, \quad v = v_{i,R} + v_{i,L}, \quad (1.55)$$

$$m = C_0 \frac{dp_0}{dt}, \quad p = p_0 + \check{p}, \quad (1.56)$$

$$m_i = C_i \frac{dp_{i,C}}{dt} = G_i p_{i,G}, \quad \check{p} = p_{i,C} + p_{i,G}. \quad (1.57)$$

See figure 1.5 for a visual representation of these equations as circuit diagrams. Note that, in these equations, viscous and thermal effects are purely local (their evolution equations do not require any spatial information), and that there is no cross-interaction between them. The values of the electronic components in the circuit are expressed as:

$$R_0(x) = \frac{\pi\mu}{S(x)^2} a_0, \quad (1.58)$$

$$L_i(x) = \frac{\rho}{S(x)} a_i, \quad R_i(x) = \frac{\pi\mu}{S(x)^2} \frac{a_i}{b_i}, \quad (1.59)$$

$$C_0(x) = \frac{S(x)(\gamma-1)}{\rho c^2}, \quad G_0(x) = \frac{\pi\kappa(\gamma-1)}{\rho^2 c^2 C_P} a_0, \quad (1.60)$$

$$C_i(x) = \frac{S(x)(\gamma-1)}{\rho c^2} a_i, \quad G_i(x) = \frac{\pi\kappa(\gamma-1)}{\rho^2 c^2 C_P} \frac{a_i}{b_i}, \quad (1.61)$$

where a_i and b_i are optimized dimensionless constants, and characteristic times $\tau_v(x) = \frac{\rho R(x)^2}{\mu}$ and $\tau_\theta(x) = \frac{\rho C_P R(x)^2}{\kappa}$ have been replaced with their expressions. Possible coefficients (a_i, b_i) are given in table 1.1.

Note that, whereas a_i and b_i are numerical constants, circuit coefficients depend on the spatial variable (except maybe G_0 and G_i in the case of constant temperature).

i	a_i	b_i
0	8	
1	5.82922×10^{-2}	2.73745×10^{-4}
2	2.00569×10^{-3}	3.28431×10^{-7}
Coefficients for $N = 2$		
i	a_i	b_i
0	8	
1	1.78820×10^{-1}	4.89408×10^{-3}
2	2.25297×10^{-2}	8.06116×10^{-5}
3	2.95706×10^{-3}	1.39782×10^{-6}
4	4.22796×10^{-4}	2.29578×10^{-8}
Coefficients for $N = 4$		

i	a_i	b_i
0	8	
1	2.09823×10^{-1}	2.47486×10^{-2}
2	7.25446×10^{-2}	2.82534×10^{-3}
3	2.47234×10^{-2}	3.30486×10^{-4}
4	8.48265×10^{-3}	3.90828×10^{-5}
5	2.91983×10^{-3}	4.63950×10^{-6}
6	1.00647×10^{-3}	5.51688×10^{-7}
7	3.50510×10^{-4}	6.52003×10^{-8}
8	1.76448×10^{-4}	5.16962×10^{-9}
Coefficients for $N = 8$		

Table 1.1: Coefficients (a_i, b_i) , optimized for $M = 100$ values of ζ ranging from 2 to 9×10^7 , covering radii of 5×10^{-4} m to 0.1 m and frequencies of 20 Hz to 2×10^4 Hz.

Summarized model

We can eliminate variables that do not store energy, in order to obtain the following system of equations:

$$\left\{ \begin{array}{l} \partial_x p + \frac{\rho}{S} \partial_t v + R_0 v + \sum_{i=1}^N R_i (v - v_{i,L}) = 0, \\ \partial_x v + \frac{S}{\rho c^2} \partial_t p + G_0 (p - p_0) + \sum_{i=1}^N G_i (p - p_0 - p_{i,C}) = 0, \\ L_i \frac{dv_{i,L}}{dt} + R_i (v_{i,L} - v) = 0, \\ C_0 \frac{dp_0}{dt} + G_0 (p_0 - p) + \sum_{i=1}^N G_i (p_{i,C} + p_0 - p) = 0, \\ C_i \frac{dp_{i,C}}{dt} + G_i (p_{i,C} + p_0 - p) = 0. \end{array} \right. \quad (1.62)$$

By further replacing the circuit components by their values, we can write:

$$\left\{ \begin{array}{l} \partial_x p + \frac{\rho}{S} \partial_t v + \frac{\pi \mu}{S^2} \left(a_0 v + \sum_{i=1}^N \frac{a_i}{b_i} (v - v_{i,L}) \right) = 0, \\ \partial_x v + \frac{S}{\rho c^2} \partial_t p + \frac{\pi \kappa (\gamma - 1)}{\rho^2 c^2 C_P} \left(a_0 (p - p_0) + \sum_{i=1}^N \frac{a_i}{b_i} (p - p_0 - p_{i,C}) \right) = 0, \\ \frac{\rho S}{\pi \mu} b_i \frac{dv_{i,L}}{dt} + (v_{i,L} - v) = 0, \\ \frac{\rho C_P S}{\pi \kappa} \frac{dp_0}{dt} + a_0 (p_0 - p) + \sum_{i=1}^N \frac{a_i}{b_i} (p_{i,C} + p_0 - p) = 0, \\ \frac{\rho C_P S}{\pi \kappa} b_i \frac{dp_{i,C}}{dt} + (p_{i,C} + p_0 - p) = 0. \end{array} \right. \quad (1.63)$$

This last system can be well-suited for direct use. For ease of notation, we will however keep the electronic symbols in the study of the model.

Energy balance of the time-domain system

System (1.52), along with the formulas of the electronic circuit, imply an energy balance equation. The first equation is multiplied by v , and the second by p , to obtain:

$$\begin{cases} \frac{\rho}{S} v \partial_t v + v \Delta + v \partial_x p = 0, \\ \frac{S}{\rho c^2} p \partial_t p + pm + p \partial_x v = 0. \end{cases} \quad (1.64)$$

The first term of each line can be put in conservative form : $v \partial_t v = \frac{1}{2} \partial_t (v^2)$. The last terms sum to $\partial_x (pv)$. The remaining terms correspond to our model of losses; their contribution can be seen as the power brought into the electronic circuit. Using equations (1.53)-(1.57) we obtain:

$$\begin{cases} v \Delta = R_0 v^2 + \sum_{i=1}^N \left(R_i v_{i,R}^2 + \frac{L_i}{2} \frac{dv_{i,L}^2}{dt} \right) \\ pm = \frac{C_0}{2} \frac{dp_0^2}{dt} + G_0 \check{p}^2 + \sum_{i=1}^N \left(G_i p_{i,G}^2 + \frac{C_i}{2} \frac{dp_{i,C}^2}{dt} \right) \end{cases}$$

Taking the sum of all equations from (1.64) and (1.2.3), and taking the integral on Ω at fixed time t yields the energy balance:

$$\frac{d}{dt} \mathcal{E} + Q + p(\Omega_{(+)})v(\Omega_{(+)}) - p(\Omega_{(-)})v(\Omega_{(-)}) = 0, \quad (1.65)$$

$$\mathcal{E} = \frac{1}{2} \int_{\Omega} \left(\frac{\rho}{S} v^2 + \frac{S}{\rho c^2} p^2 + C_0 p_0^2 + \sum_{i=1}^N C_i p_{i,C}^2 + \sum_{i=1}^N L_i v_{i,L}^2 \right), \quad (1.66)$$

$$Q = \int_{\Omega} \left(R_0 v^2 + \sum_{i=1}^N R_i v_{i,R}^2 + G_0 \check{p}^2 + \sum_{i=1}^N G_i p_{i,G}^2 \right) \quad (1.67)$$

We see that the expression of the energy is a modification of that of a lossless pipe. The lossless case is recovered when all a_i are zero, which results in $\Delta = m = 0$.

1.2.4 Finite elements discretization in space

From the time-domain system, it is possible to deduce a numerical scheme simulating wave propagation with viscothermal losses.

We consider system (1.52) to be defined on a segment $\Omega \subset \mathbb{R}$, with pressure p in function space $H^1(\Omega)$ and flow v in $L^2(\Omega)$. The variational formulation of

system (1.52) is:

$$\begin{aligned} & \forall \tilde{v} \in L^2(\Omega), \forall \tilde{p} \in H^1(\Omega), \\ & \begin{cases} \int_{\Omega} \frac{\rho}{S} \partial_t v \tilde{v} + \int_{\Omega} \Delta(x) \tilde{v}(x) + \int_{\Omega} \partial_x p \tilde{v} = 0, \\ \int_{\Omega} \frac{S}{\rho c^2} \partial_t p \tilde{p} + \int_{\Omega} m(x) \tilde{p}(x) - \int_{\Omega} \partial_x \tilde{p} v + \lambda_{(-)} \tilde{p}(\Omega_{(-)}) + \lambda_{(+)} \tilde{p}(\Omega_{(+)}) = 0, \\ \text{B.C.}(p(\Omega_{(\pm)}), \lambda_{(\pm)}, \dots), \end{cases} \end{aligned} \quad (1.68)$$

where variables $\lambda_{(\pm)} = v(\Omega_{(\pm)}) \cdot n$ denote the exiting flow on the boundary of Ω , which is linked to the pressure through some boundary conditions “B.C.(p, λ)”.

Finite element methods make use of bilinear and linear forms. As in section 1.1, for any $v, \tilde{v} \in L^2(\Omega)$ and $p, \tilde{p} \in H^1(\Omega)$ we denote:

$$m^{L^2}(v, \tilde{v}) := \int_{\Omega} \frac{\rho}{S} v \tilde{v} \quad (1.69)$$

$$m^{H^1}(p, \tilde{p}) := \int_{\Omega} \frac{S}{\rho c^2} p \tilde{p} \quad (1.70)$$

$$b(p, v) := - \int_{\Omega} v \partial_x p \quad (1.71)$$

$$e_{(\pm)}(p) := p(\Omega_{(\pm)}) \quad (1.72)$$

Similarly, we assimilate the circuit coefficients with the corresponding bilinear forms:

$$R_0(v, \tilde{v}) := \int_{\Omega} R_0 v \tilde{v}, \quad L_i(v, \tilde{v}) := \int_{\Omega} L_i v \tilde{v}, \quad (1.73)$$

$$C_0(p, \tilde{p}) := \int_{\Omega} C_0 p \tilde{p}, \quad G_0(p, \tilde{p}) := \int_{\Omega} G_0 p \tilde{p}, \quad (1.74)$$

and so on for R_i, C_i and G_i .

Variables p and v are discretized in space with 1D spectral finite elements, as in [11]. We replace spaces $H^1(\Omega)$ and $L^2(\Omega)$ with finite-dimensional spaces V_h and W_h , constructed with one-dimensional spectral finite elements [44]. That is, V_h and W_h are spanned by their respective bases $\{\phi_k\}_{k=1 \dots n_{H^1}}, \{\psi_k\}_{k=1 \dots n_{L^2}}$ of Lagrange interpolation polynomials, and the bilinear forms m^{L^2}, m^{H^1}, b , and the circuit elements are approximated using a quadrature procedure for mass lumping.

Pressure p uses V_h basis functions $\{\phi_k\}$, for which the degrees of freedom at element boundaries are not duplicated, whereas v uses W_h basis functions $\{\psi_k\}$, with duplicated degrees of freedom. Fields $\Delta, v_{i,R}$ and $v_{i,L}$ are discretized accordingly in W_h , whereas $m, p_0, \check{p}, p_{i,G}$ and $p_{i,C}$ are set to be in V_h .

In order to reduce the number of variables, we eliminate the variables that do not store energy. Let us denote V, P, V_i, P_0 and P_i the respective coordinate

decompositions of v , p , $v_{i,L}$, p_0 and $p_{i,C}$.

$$\begin{aligned} v(x, t) &= \sum_{k=1}^{n_{L^2}} (V(t))_k \psi_k(x), & v_{i,L}(x, t) &= \sum_{k=1}^{n_{L^2}} (V_i(t))_k \psi_k(x), \\ p(x, t) &= \sum_{k=1}^{n_{H^1}} (P(t))_k \phi_k(x), & p_0(x, t) &= \sum_{k=1}^{n_{H^1}} (P_0(t))_k \phi_k(x), \\ p_{i,C}(x, t) &= \sum_{k=1}^{n_{H^1}} (P_i(t))_k \phi_k(x). \end{aligned}$$

All interpolation nodes and quadrature points are chosen to be Gauss-Lobato points. These choices allow us to use approximate lumped mass matrices, without any consistency loss [44]. We also evaluate the circuit coefficients in this way.

$$\begin{aligned} M_{kl}^{L^2} &:= \int_{\Omega} \frac{\rho}{S} \psi_k \psi_l & M_{kl}^{L^2} &= 0 \text{ for } k \neq l \\ M_{kl}^{H^1} &:= \int_{\Omega} \frac{S}{\rho c^2} \phi_k \phi_l & M_{kl}^{H^1} &= 0 \text{ for } k \neq l \\ B_{kl} &:= - \int_{\Omega} \psi_k \partial_x \phi_l, & B_{kl} &= 0 \text{ if } \psi_k \text{ and } \phi_l \text{ on different elements,} \\ (R_0)_{kl} &:= \int_{\Omega} R_i \psi_k \psi_l, & (R_0)_{kl} &= 0 \text{ for } k \neq l, \\ (C_0)_{kl} &:= \int_{\Omega} R_i \phi_k \phi_l, & (C_0)_{kl} &= 0 \text{ for } k \neq l, \end{aligned}$$

and similarly for the other circuit elements. Here \int represents the approximate integral computed with a quadrature formula, such that the mass and circuit matrices become diagonal. We define the endpoint evaluation vectors:

$$E_{(\pm)} = (e_{(\pm)}(\phi_k))_k, \quad \text{i.e.} \quad E_{(-)} = \begin{pmatrix} 1 \\ 0 \\ \vdots \\ 0 \end{pmatrix}, \quad E_{(+)} = \begin{pmatrix} 0 \\ \vdots \\ 0 \\ 1 \end{pmatrix}$$

Vectors $E_{(\pm)}$ are used to evaluate the endpoint values of $P \in V_h$: the associated linear forms are expressed as $e_{(\pm)}(P) = E_{(\pm)}^* P$. Given the space discretization we have chosen, the representation of $E_{(\pm)}$ on the (ϕ_k) basis contains a single 1 on the first (or last) degree of freedom of the segment Ω . The resulting system of

equations is:

$$\left\{ \begin{array}{l} M^{L^2} \partial_t V + R_0 V + \sum_{i=1}^N R_i (V - V_i) - BP = 0 \\ M^{H^1} \partial_t P + G_0 (P - P_0) + \sum_{i=1}^N G_i (P - P_0 - P_i) \\ \quad + B^* V + \lambda_{(-)} E_{(-)} + \lambda_{(+)} E_{(+)} = 0 \\ L_i \partial_t V_i + R_i (V_i - V) = 0, \\ C_0 \partial_t P_0 + G_0 (P_0 - P) + \sum_{i=1}^N G_i (P_i + P_0 - P) = 0, \\ C_i \partial_t P_i + G_i (P_i + P_0 - P) = 0. \\ \text{B.C.} (E_{(\pm)}^* P, \lambda_{(\pm)}, \dots) \end{array} \right. \quad (1.75)$$

The total dimension of the unknown variables is $(N + 1)n_{L^2} + (N + 2)n_{H^1}$.

1.2.5 Time discretization

For discretization in time, we use an interleaved scheme similar to [8]. We denote by Δt the time step, and n the step number, so that $t = n\Delta t$. Unknowns P, P_0 and P_i are evaluated at integer times $(0, 1, 2, \dots)$, whereas V and V_i are evaluated on a staggered grid $(1/2, 3/2, 5/2, \dots)$.

The scheme is written simply by rewriting system (1.75), replacing time differentiation with its discrete counterpart δ , and adding operator μ where necessary. The operators were defined in section 1.1.4.

$$\left\{ \begin{array}{l} M^{L^2} \delta V^n + R_0 \mu V^n + \sum_{i=1}^N R_i \mu (V - V_i)^n - BP^n = 0 \\ M^{H^1} \delta P^{n+1/2} + G_0 \mu (P - P_0)^{n+1/2} + \sum_{i=1}^N G_i \mu (P - P_0 - P_i)^{n+1/2} \\ \quad + B^* V^{n+1/2} + \lambda_{(-)}^{n+1/2} E_{(-)} + \lambda_{(+)}^{n+1/2} E_{(+)} = 0 \\ L_i \delta V_i^n + R_i \mu (V_i - V)^n = 0, \\ C_0 \delta P_0^{n+1/2} + G_0 \mu (P_0 - P)^{n+1/2} + \sum_{i=1}^N G_i \mu (P_i + P_0 - P)^{n+1/2} = 0, \\ C_i \delta P_i^{n+1/2} + G_i \mu (P_i + P_0 - P)^{n+1/2} = 0. \\ \text{B.C.} (E_{(\pm)}^* \mu P^{n+1/2}, \lambda_{(\pm)}^{n+1/2}, \dots) \end{array} \right. \quad (1.76)$$

This is in fact almost the same scheme as in [8], but our spatial discretization uses finite elements instead of finite differences, and our choice of coefficients is different. Here it is written in implicit form, but it can be made explicit with a Schur complement.

1.2.6 Energy balance

Let us show that the scheme is stable under the same condition as for the lossless pipe. This statement was proved in [8] for a similar scheme, using the notion of modified energy; here we derive the energy balance directly. In all this section, we will use $\|\cdot\|_W$, where W is a symmetric definite positive matrix, to denote a weighted norm. For instance:

$$\begin{aligned}\|P\|_{M^{H^1}} &:= P^* M^{H^1} P, \\ \|V\|_{L_i} &:= V^* L_i V,\end{aligned}$$

and so on. For convenience, let us reintroduce the circuit variables in discretized form:

$$\begin{aligned}\Delta^n &= \Delta_0^n + \sum_{i=1}^N \Delta_i^n, & m^{n+1/2} &= m_0^{n+1/2} + \sum_{i=1}^N m_i^{n+1/2}, \\ \Delta_0^n &= R_0 \mu V^n, & m_0^{n+1/2} &= G_0 \mu \check{P}^{n+1/2}, \\ \Delta_i^n &= R_i \mu V_{i,R}^n = L_i \delta V_i^n, & V^{n+1/2} &= V_{i,R}^{n+1/2} + V_i^{n+1/2}, \\ m^{n+1/2} &= C_0 \delta P_0^{n+1/2}, & P^n &= P_0^n + \check{P}^n, \\ m_i^{n+1/2} &= C_i \delta P_i^{n+1/2} = G_i \mu P_{i,G}^{n+1/2}, & \check{P}^n &= P_i^n + P_{i,G}^n.\end{aligned}$$

With these variables and equations, the evolution of V and P can be rewritten as:

$$\begin{cases} M^{L^2} \delta V^n + \Delta^n - B P^n = 0 \\ M^{H^1} \delta P^{n+1/2} + m^{n+1/2} + B^* V^{n+1/2} + \lambda_{(-)}^{n+1/2} E_{(-)} + \lambda_{(+)}^{n+1/2} E_{(+)} = 0 \end{cases}$$

Since this scheme is only a slight modification of that for a lossless pipe, we expect to obtain the same expression for the energies of P and V , and also the same stability condition, namely:

$$\begin{aligned}\mathcal{E}_P^n &= \frac{1}{2} \|P^n\|_{M^{H^1}}, \\ \mathcal{E}_V^n &= \frac{1}{2} \|\mu V^n\|_{M^{L^2}}, \\ \mathcal{E}_{P+V}^n &= \frac{1}{2} \|P^n\|_{M_{\Delta t}^{H^1}} + \frac{1}{2} \|\mu V^n\|_{M^{L^2}},\end{aligned}\tag{1.77}$$

where $M_{\Delta t}^{H^1}$ was the *modified mass matrix* resulting in the stability condition from equation (1.31). Note that the matrix is positive if and only if the CFL condition (1.32) holds. In order to make these energies appear, we multiply the second equation by μP ; whereas to the first we apply μ and multiply by $\mu \mu V$. All terms are implicitly centered on $n + 1/2$.

$$\begin{aligned}(\mu P)^* M^{H^1} \delta P + (\mu P)^* m + (\mu P)^* B^* V \\ + \lambda_{(-)} E_{(-)}^* \mu P + \lambda_{(+)} E_{(+)}^* \mu P = 0, \\ (\mu \mu V)^* M^{L^2} \mu \delta V + (\mu \mu V)^* \mu \Delta - (\mu \mu V)^* B \mu P = 0.\end{aligned}$$

Using property (1.21), we recognize the variations of energy $\delta\mathcal{E}_P$ and $\delta\mathcal{E}_V$, and the source term $S = -\lambda_{(-)}E_{(-)}^*\mu P - \lambda_{(+)}E_{(+)}^*\mu P$ corresponding to the energy exchange at the boundary. Since we are dealing with real scalars, dot products are symmetric, so $(\mu P)^*B^*V = V^*B\mu P$, and thus

$$\delta\mathcal{E}_P + \delta\mathcal{E}_V + (\mu P)^*m + (\mu\mu V)^*\mu\Delta + (V - \mu\mu V)^*B\mu P = S.$$

Note that $\mu\mu V = V + \frac{\Delta t^2}{4}\delta\delta V$, as a result of the definitions of μ and δ . Thus, by applying the evolution equation of V , and (1.21) again, we get

$$(V - \mu\mu V)^*B\mu P = -\frac{\Delta t^2}{8}\delta\|BP\|_{(M^{L^2})^{-1}} + \frac{\Delta t^2}{4}(\delta\Delta)^*(M^{L^2})^{-1}B\mu P.$$

The first term corresponds to the stability condition. For the second term, we apply the equation again to find that

$$\frac{\Delta t^2}{4}(\delta\Delta)^*(M^{L^2})^{-1}B\mu P = \delta\epsilon_\Delta + \frac{\Delta t^2}{4}(\delta\Delta)^*\mu\delta V,$$

where a small energy ϵ_Δ has been isolated:

$$\epsilon_\Delta = \frac{\Delta t^2}{8}\|\Delta\|_{(M^{L^2})^{-1}}. \quad (1.78)$$

Finally we regroup all terms involving Δ and V by remarking the following identity (a consequence of the definitions of μ and δ):

$$(\mu\mu V)^*\mu\Delta + \frac{\Delta t^2}{4}(\delta\Delta)^*\mu\delta V = \mu((\mu V)^*\Delta).$$

Thus the energy balance can be written as:

$$\delta\mathcal{E}_{P+V} + \delta\epsilon_\Delta + (\mu P)^*m + \mu((\mu V)^*\Delta) = S. \quad (1.79)$$

Finally, it is easy to see that each circuit individually verifies an energy balance:

$$\delta\mathcal{E}_{\text{therm}} + Q_{\text{therm}} - (\mu P)^*m = 0, \quad (1.80)$$

$$\delta\mathcal{E}_{\text{visc}} + Q_{\text{visc}} - (\mu V)^*\Delta = 0, \quad (1.81)$$

where the stored energies and dissipated powers are given by:

$$\mathcal{E}_{\text{therm}}^n = \frac{1}{2}\|P_0^n\|_{C_0} + \sum_{i=1}^N \frac{1}{2}\|P_i^n\|_{C_i}, \quad (1.82)$$

$$Q_{\text{therm}}^{n+1/2} = \left\| \mu(P - P_0)^{n+1/2} \right\|_{G_0} + \sum_{i=1}^N \left\| \mu(P_i + P_0 - P)^{n+1/2} \right\|_{G_i}, \quad (1.83)$$

$$\mathcal{E}_{\text{visc}}^{n+1/2} = \sum_{i=1}^N \frac{1}{2} \left\| V_i^{n+1/2} \right\|_{L_i}, \quad (1.84)$$

$$Q_{\text{visc}}^n = \|\mu V^n\|_{R_0} + \sum_{i=1}^N \|\mu(V_i - V)^n\|_{R_i}. \quad (1.85)$$

The viscous energy balance (1.81) must be averaged over two time steps, to compensate the exchange term $\mu((\mu V)^* \Delta)$. In conclusion, the global energy balance is:

$$\delta \mathcal{E}_{\text{total}}^{n+1/2} + Q_{\text{total}}^{n+1/2} = S^{n+1/2}, \quad (1.86)$$

$$\mathcal{E}_{\text{total}}^n = \mathcal{E}_{P+V}^n + \mathbf{e}_{\Delta}^n + \mathcal{E}_{\text{therm}}^n + \mu \mathcal{E}_{\text{visc}}^n, \quad (1.87)$$

$$Q_{\text{total}}^{n+1/2} = Q_{\text{therm}}^{n+1/2} + \mu Q_{\text{visc}}^{n+1/2}, \quad (1.88)$$

$$S^{n+1/2} = -\lambda_{(-)}^{n+1/2} E_{(-)}^* \mu P^{n+1/2} - \lambda_{(+)}^{n+1/2} E_{(+)}^* \mu P^{n+1/2}. \quad (1.89)$$

The condition of positivity of this energy is the same as for the lossless pipe. Indeed, all energy contributions of viscous and thermal effect lead to positive terms, whereas \mathcal{E}_{P+V} is positive under the same condition as before:

$$\Delta t < 2 \left[\rho \left((M^{H^1})^{-1} B^* M^{L^2} B \right) \right]^{-\frac{1}{2}}. \quad (1.90)$$

The energy exchange with neighbouring elements is the same as before, which means that this scheme can be combined in an energy-consistent way with all elements presented in chapter 2.

Chapter 2

Around the Pipes

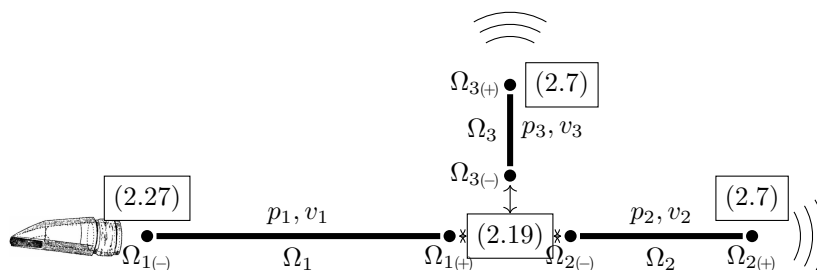


Figure 2.1: A possible one-hole instrument

In chapter 1, we present numerical schemes allowing time-domain simulation of a variable-section pipe with no holes, which is well-behaved in terms of energy. To obtain a complete instrument, we need to manage radiation of sound, to drill tone holes, and to attach a mouthpiece.

The model used for the pipes cannot account for exchange of air on the lateral sides of a pipe. Tone holes must therefore be taken into account as side-pipes, with a T-shaped junction emerging from the main bore. Such an idea had been proposed in [40] with simplified models of pipe and junction to be used with digital waveguides. Hence we will call “pipe” the length of tubing of the main bore between the source mechanism and a tone hole, between two consecutive holes, or even the small length corresponding to a hole itself¹. Each pipe may have a variable section along its length, but we suppose axisymmetry and plane-wave propagation in each pipe.

At the end of each pipe, boundary conditions will be placed, which may interact with complex elements (see figure 2.1): for instance, a reed model will connect to one end of the first pipe, a three-way junction will connect each tone hole to consecutive sections of the main pipe, and an impedance model will be placed at the exit of each tone hole and at the end of the instrument. We detail below the models used for each element. Pipes were discretized with finite elements methods, whereas all boundary conditions only depend on a finite

¹We directly model propagation in a tone hole as in any other pipe, which allows us to consider undercut tone holes of arbitrary shape.

number of variables. Explicit numerical schemes are given for all elements, for each of which a numerical energy balance is verified, allowing stable and accurate simulation of instruments with arbitrary topology.

Let us start with the simplest possible boundary conditions, before moving on to models of radiation, junction and reed. Since both ends of a pipe behave in exactly the same way, and boundary conditions can interact with either, we will consider “(+)” or “(-)” to be always implicitly the same.

For all types of boundary conditions, we must carefully take into account the work $\lambda^{n+1/2} E^* \mu P^{n+1/2}$ exchanged between the pipe and its boundary condition. For energy conservation, it must be exactly compensated, as any slight error on the work could cause accumulating variations of energy.

2.1 Boundary conditions

2.1.1 Flow condition

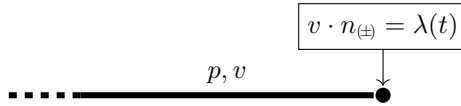


Figure 2.2: Flow condition at the end of a pipe

The most straightforward boundary condition is when $\lambda = \lambda(t)$ is given, for instance $\lambda(t) = 0$ in the case of a homogeneous Dirichlet boundary condition on flow (which corresponds to a Neumann condition on pressure). In that case, its work on the pipe is:

$$W(t) = -c(p(t))\lambda(t)$$

in the continuous case. Simply setting

$$\lambda^{n+1/2} = \lambda((n + 1/2)\Delta t) \tag{2.1}$$

gives the discrete analog:

$$W^{n+1/2} = -\lambda^{n+1/2} E^* \mu P^{n+1/2}.$$

In particular, if $\lambda(t) = 0$, the boundary condition exerts no work on the pipe, as expected.

2.1.2 Pressure condition

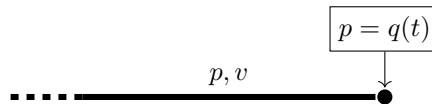


Figure 2.3: Pressure condition at the end of a pipe

A more subtle boundary condition is to enforce the value of the pressure to follow a given function $q(t)$ (Dirichlet boundary condition on the pressure, or Neumann on flow):

$$c(p(t)) := q(t).$$

The discrete analog is to ensure that $E^* \mu P^{n+1/2} = q^{n+1/2}$, where $q^{n+1/2}$ corresponds to $q(t)$ evaluated at the appropriate time $t = (n + 1/2)\Delta t$.

Explicit computations

At first glance, this boundary condition seems implicit, since $\mu P^{n+1/2}$ depends on the unknown values of $\lambda_{(\pm)}^{n+1/2}$. However, from the evolution equation of P in the scheme², $E^* \mu P^{n+1/2}$ can be written as:

$$E^* \mu P^{n+1/2} = p_{\text{no flow}}^{n+1/2} - \frac{\Delta t}{2} \frac{\lambda^{n+1/2}}{m_{\text{end}}}, \quad (2.2)$$

where only one boundary condition appears thanks to the fact that M^{H^1} is diagonal. Here we denote

$$p_{\text{no flow}}^{n+1/2} = E^* P^n - \frac{\Delta t}{2} E^* (M^{H^1})^{-1} B^* V^{n+1/2}, \quad (2.3)$$

$$m_{\text{end}} = E^* M^{H^1} E. \quad (2.4)$$

Thus $p_{\text{no flow}}^{n+1/2}$ is the value that $E^* \mu P^{n+1/2}$ would take if there was no flow $\lambda^{n+1/2}$, and m_{end} is the inertia of the last degree of freedom.

Since we want that $E^* \mu P^{n+1/2} = q^{n+1/2}$, the appropriate flow is:

$$\lambda^{n+1/2} = \frac{2m_{\text{end}}}{\Delta t} (p_{\text{no flow}}^{n+1/2} - q^{n+1/2}), \quad (2.5)$$

which can be computed from previously-known data P^n and $V^{n+1/2}$.

Energy balance

As before, the resulting work is expressed simply as:

$$W^{n+1/2} = -\lambda^{n+1/2} E^* \mu P^{n+1/2} = -\lambda^{n+1/2} q^{n+1/2}.$$

In particular, if $q = 0$, the boundary condition does not exchange energy with the pipe.

2.1.3 Radiation impedance

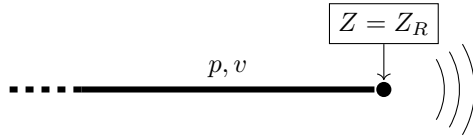


Figure 2.4: Radiation impedance at the end of a pipe

Every opening of the instrument, be it a bell or a tone hole, radiates energy into the surrounding air. The corresponding boundary condition is not obvious,

²Here we assume the lossless scheme is used. For the scheme with viscothermal losses, we can still express $E^* \mu P$ as $p_{\text{no flow}} + \frac{\Delta t}{2m_{\text{end}}} \lambda$, but the expressions of $p_{\text{no flow}}$ and m_{end} are more complex.

but for one-dimensional propagation models it is characterized by the *radiation impedance*, which has been studied in various cases [3, 16, 29]. One standard model of radiation impedance depends on two parameters:

$$Z_R = Z^+ \left[j\delta ka + \frac{1}{2}\beta_0(ka)^2 \right],$$

where $k = \frac{\omega}{c}$ is the wave number, $Z^+ = \frac{\rho c}{\pi a^2}$ is the characteristic impedance, a is the radius of the radiating exit, and δ and β_0 are two positive empirical constants. Both flanged and unflanged radiation can be put in this form at low frequencies. Directly using this expression in the time domain would however result in instabilities: that is why we instead use a Padé approximation. We introduce two new positive constants α and β , and set (according to our sign convention):

$$\frac{p}{v \cdot n} = Z_R = Z^+ \frac{j\omega}{\alpha + j\omega\beta} \quad \text{at the end of the pipe.} \quad (2.6)$$

In the time domain, this can be rephrased as:

$$\partial_t v \cdot n = \frac{\alpha}{Z^+} p + \frac{\beta}{Z^+} \partial_t p. \quad (2.7)$$

Time-domain radiation model

We introduce a new variable:

$$\zeta := -\frac{v \cdot n}{\sqrt{\alpha}} + \frac{\beta}{Z^+ \sqrt{\alpha}} p, \quad (2.8)$$

so that the evolution equation of ζ eliminates the $\partial_t p$ component:

$$\partial_t \zeta = -\frac{\sqrt{\alpha}}{Z^+} p. \quad (2.9)$$

The scaling choice for ζ is due to energy concerns which will appear below. With this new variable, we can express the flow as

$$\lambda = -\sqrt{\alpha} \zeta + \frac{\beta}{Z^+} p. \quad (2.10)$$

Our radiation model is summarized in the following system:

$$\begin{cases} Z^+ \partial_t \zeta + \sqrt{\alpha} p = 0 \\ \lambda + \sqrt{\alpha} \zeta - \frac{\beta}{Z^+} p = 0 \end{cases} \quad (2.11)$$

Before deducing the corresponding numerical scheme, let us write the energy balance. Each equation from the system above is multiplied by the appropriate value:

$$\begin{cases} \frac{Z^+}{2} \partial_t \zeta^2 + \sqrt{\alpha} \zeta p = 0 \\ -\lambda p - \sqrt{\alpha} \zeta p + \frac{\beta}{Z^+} p^2 = 0, \end{cases} \quad (2.12)$$

so that the energy balance is:

$$\mathcal{E}_{\text{rad}} = \frac{Z^+}{2} \zeta^2 \quad (2.13)$$

$$\frac{d}{dt} \mathcal{E}_{\text{rad}} = \lambda p - \frac{\beta}{Z^+} p^2. \quad (2.14)$$

The radiation model thus exchanges energy with the pipe as expected, but also stores some and dissipates some. The energy storage can be seen in the conservative term $\frac{d}{dt} \mathcal{E}_{\text{rad}}$, and the dissipation in the negative term $-\frac{\beta}{Z^+} p^2$.

Numerical scheme

The numerical scheme corresponding to (2.11) can be immediately deduced:

$$\begin{cases} Z^+ \frac{\zeta^{n+1} - \zeta^n}{\Delta t} + \sqrt{\alpha} E^* \mu P^{n+1/2} = 0, \\ \lambda^{n+1/2} + \sqrt{\alpha} \bar{\zeta}^{n+1/2} - \frac{\beta}{Z^+} E^* \mu P^{n+1/2} = 0. \end{cases} \quad (2.15)$$

Energy balance

Let us write the discrete analog of equation (2.12) for our radiation scheme (2.15):

$$\begin{cases} \frac{Z^+}{2} \frac{(\zeta^{n+1})^2 - (\zeta^n)^2}{2} + \sqrt{\alpha} \bar{\zeta}^{n+1/2} E^* \mu P^{n+1/2} = 0 \\ -\lambda^{n+1/2} E^* \mu P^{n+1/2} - \sqrt{\alpha} \bar{\zeta}^{n+1/2} E^* \mu P^{n+1/2} + \frac{\beta}{Z^+} (E^* \mu P^{n+1/2})^2 = 0. \end{cases} \quad (2.16)$$

The resulting discrete energy balance is:

$$\mathcal{E}_{\text{rad}}^n = \frac{Z^+}{2} (\zeta^n)^2 \quad (2.17)$$

$$\frac{\mathcal{E}_{\text{rad}}^{n+1} - \mathcal{E}_{\text{rad}}^n}{\Delta t} = \lambda^{n+1/2} E^* \mu P^{n+1/2} - \frac{\beta}{Z^+} (E^* \mu P^{n+1/2})^2. \quad (2.18)$$

As expected, the element exchanges work with the pipe, stores some in variable ζ , and dissipates some.

Schur complement

As shown before in equation (2.2), we know in advance that

$$E^* \mu P^{n+1/2} = p_{\text{no flow}}^{n+1/2} - \frac{\Delta t}{2m_{\text{end}}} \lambda^{n+1/2},$$

where $p_{\text{no flow}}^{n+1/2}$ is defined by equation (2.3). Hence there are only two unknowns in the linear system (2.15). It is possible to solve it explicitly to find the following

expressions for ζ^{n+1} and $\lambda^{n+1/2}$:

$$\begin{aligned}\mu_{\Delta t} &:= 1 + \frac{\Delta t}{2} \frac{\beta}{Z^+ m_{\text{end}}}, & \nu_{\Delta t} &:= 1 + \frac{\Delta t^2}{4} \frac{\alpha}{\mu_{\Delta t} m_{\text{end}} Z^+}, \\ \bar{\zeta}^{n+1/2} &= \frac{1}{\nu_{\Delta t}} \left(\zeta^n - \frac{\Delta t}{2\mu_{\Delta t}} \frac{\sqrt{\alpha}}{Z^+} p_{\text{no flow}}^{n+1/2} \right), & \zeta^{n+1} &= 2\bar{\zeta}^{n+1/2} - \zeta^n, \\ \lambda^{n+1/2} &= \frac{1}{\mu_{\Delta t}} \left(\frac{\beta}{Z^+} p_{\text{no flow}}^{n+1/2} - \sqrt{\alpha} \bar{\zeta}^{n+1/2} \right).\end{aligned}$$

Most of these values need not be computed every time. By calculating coefficients in advance, deducing $\bar{\zeta}^{n+1/2}$ and $\lambda^{n+1/2}$ from $p_{\text{no flow}}^{n+1/2}$ takes only four multiplications and two additions.

2.1.4 Opening and closing holes

The scaling chosen for ζ is such that α does not appear in the energy balance, and β appears only in the losses. This makes it possible to let them vary in time without any risk for stability of the scheme (as long as β remains nonnegative), simply by replacing the corresponding symbols with $\alpha^{n+1/2}$ and $\beta^{n+1/2}$ in all equations above. Therefore we can open and close holes during the simulation, and transient behavior should be accurately reproduced.

It is a work in progress to know exactly how α and β should vary in order to represent the influence of a finger or key pad approaching the hole.

2.2 Junction of three pipes

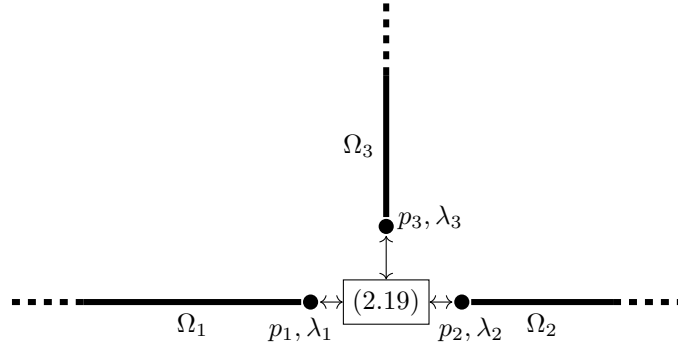


Figure 2.5: Tone holes are modeled as short pipes connected to the side of the main bore.

We now consider a single junction of three pipes, as illustrated in figure 2.5. Up to renaming, let us suppose the connected pipes are Ω_1 and Ω_2 for the body of the instrument, and Ω_3 for the hole. At the junction, we assume slightly refined Kirchhoff relations, derived from section 7.7 of [12]. They consist in

continuity of the flow, and two relations between pressure and speed:

$$\begin{cases} \lambda_1 + \lambda_2 + \lambda_3 = 0 \\ p_1 - (m_{11} - m_{12})\partial_t \lambda_1 = p_2 - (m_{22} - m_{12})\partial_t \lambda_2, \\ p_1 - (m_{11} - m_{12})\partial_t \lambda_1 = p_3 - m_{12}\partial_t \lambda_3. \end{cases} \quad (2.19)$$

As before, λ_i denotes the outwards velocity $\lambda_i = v_i(\Omega_i^{(\pm)}) \cdot n_i^{(\pm)}$ where n_i is the outwards-pointing unit vector ; and $p_i = p_i(\Omega_i)$ is the pressure at the end of each waveguide. This system can be rewritten:

$$\begin{cases} \lambda_3 = -\lambda_1 - \lambda_2 \\ m_{11}\partial_t \lambda_1 + m_{12}\partial_t \lambda_2 - p_1 + p_3 = 0, \\ m_{12}\partial_t \lambda_1 + m_{22}\partial_t \lambda_2 - p_2 + p_3 = 0. \end{cases} \quad (2.20)$$

2.2.1 Assembled version

It is convenient to assemble this system into a vector equation. Let us introduce two new variables γ_1, γ_2 , and denote:

$$\gamma = \begin{pmatrix} \gamma_1 \\ \gamma_2 \end{pmatrix}, \quad M_J = \begin{pmatrix} m_{11} & m_{12} \\ m_{12} & m_{22} \end{pmatrix}, \quad T_J = \begin{pmatrix} 1 & 0 & -1 \\ 0 & 1 & -1 \end{pmatrix},$$

$$\lambda_{123} = \begin{pmatrix} \lambda_1 \\ \lambda_2 \\ \lambda_3 \end{pmatrix}, \quad p_{123} = \begin{pmatrix} p_1 \\ p_2 \\ p_3 \end{pmatrix}.$$

Then we express system (2.20) as:

$$\begin{cases} \lambda_{123} = -T_J^* \gamma, \\ M_J \partial_t \gamma + T_J p_{123} = 0. \end{cases} \quad (2.21)$$

The power emitted from the junction should be $\lambda_{123}^* p_{123}$. From system (2.21), using the symmetry of M_J , we deduce:

$$\frac{1}{2} \frac{d}{dt} (\gamma^* M_J \gamma) + \gamma^* T_J p_{123} = 0.$$

Note that $\gamma^* T_J$ is the same as $-\lambda_{123}^*$, and so the second term corresponds to the exchanged power. Thus the energy balance of the junction is:

$$\mathcal{E}_{\text{junc}} = \frac{1}{2} \gamma^* M_J \gamma, \quad (2.22)$$

$$\frac{d}{dt} \mathcal{E}_{\text{junc}} = p_1 \lambda_1 + p_2 \lambda_2 + p_3 \lambda_3. \quad (2.23)$$

Therefore the junction is conservative, it does not dissipate any energy. However the junction's internal energy (2.22) must be positive definite for the system to be stable, i.e. M_J must be positive definite. This gives a condition on the acoustic masses: assuming m_{11} and m_{22} are nonnegative, one must have $m_{12}^2 < m_{11} m_{22}$, i.e. the absolute value of m_{12} cannot be too large.

Remark. It is also possible to use diagonalized variables:

$$\gamma = \begin{pmatrix} \gamma_+ \\ \gamma_- \end{pmatrix}, \quad M_J = \begin{pmatrix} m_+ & 0 \\ 0 & m_- \end{pmatrix}, \quad T_J = \begin{pmatrix} \tau_{1+} & \tau_{2+} & \tau_{3+} \\ \tau_{1-} & \tau_{2-} & \tau_{3-} \end{pmatrix},$$

where the coefficients used for the change of variables are:

$$\begin{aligned} \kappa &= \frac{m_{22} - m_{11}}{2m_{12}} & D &= \kappa^2 + 1 \\ \bar{m} &= \frac{m_{11} + m_{12}}{2} & m_{\pm} &= \bar{m} \pm m_{12}\sqrt{D} \\ \tau_{1+} &= -\frac{1}{\sqrt{2}}\sqrt{1 - \frac{\kappa}{\sqrt{D}}}, & \tau_{2+} &= -\frac{1}{\sqrt{2}}\sqrt{1 + \frac{\kappa}{\sqrt{D}}}, & \tau_{3+} &= -\tau_{1+} - \tau_{2+}, \\ \tau_{1-} &= -\frac{1}{\sqrt{2}}\sqrt{1 + \frac{\kappa}{\sqrt{D}}}, & \tau_{2-} &= \frac{1}{\sqrt{2}}\sqrt{1 - \frac{\kappa}{\sqrt{D}}}, & \tau_{3-} &= -\tau_{1-} - \tau_{2-}. \end{aligned}$$

System (2.21) remains valid, and so does the energy balance (2.22). Note that M_J is positive definite if and only if $m_+ > 0$ and $m_- > 0$, which is equivalent to the above criterion.

Remark. Values of the masses m_{11}, m_{12}, m_{22} can be deduced from coefficients m_a and m_s given in [12]. However, the criterion for positivity of the energy is always violated. This is certainly due to the artificial reduction of the volume to zero. This “negative mass” is well-known by acousticians, and poses no problem when performing frequency-domain computations. Additional work will be needed to find models that are better suited to the time domain.

Our choice in the toolbox was to change the negative eigenvalue of M for a small positive one, in order to be able to get coherent results.

2.2.2 Numerical scheme

We denote by $E_i^* P_i^n$ the end-value of the pressure in pipe i , where $i = 1, 2, 3$. Discrete-time vectors are defined by:

$$\lambda_{123}^{n+1/2} = \begin{pmatrix} \lambda_1^{n+1/2} \\ \lambda_2^{n+1/2} \\ \lambda_3^{n+1/2} \end{pmatrix}, \quad \bar{p}_{123}^{n+1/2} = \begin{pmatrix} E_1^* P_1^n \\ E_2^* P_2^n \\ E_3^* P_3^n \end{pmatrix}.$$

Our numerical scheme for the junction is the discrete-time analog of (2.21):

$$\begin{cases} \lambda_{123}^{n+1/2} = -T_J^* \bar{\gamma}^{n+1/2} \\ M_J \frac{\gamma^{n+1} - \gamma^n}{\Delta t} + T_J \bar{p}_{123}^{n+1/2} = 0, \end{cases} \quad (2.24)$$

where $\bar{\gamma}^{n+1/2} = \frac{\gamma^{n+1} + \gamma^n}{2}$ as per our usual convention.

2.2.3 Energy conservation

The power emitted from the junction should be the sum of all works into the neighboring pipes $\lambda_i^{n+1/2} E_i^* \mu P_i^{n+1/2}$; it can be written as $(\lambda_{123}^{n+1/2})^* \bar{p}_{123}^{n+1/2}$. Calculations similar to before give an energy balance result:

$$\frac{(\gamma^{n+1})^* M_J \gamma^{n+1} - (\gamma^n)^* M_J \gamma^n}{2\Delta t} + (\bar{\gamma}^{n+1/2})^* T_J \bar{p}_{123}^{n+1/2} = 0,$$

hence the junction's energy is written as

$$\mathcal{E}_{\text{junc}}^n = \frac{1}{2} (\gamma^n)^* M_J \gamma^n, \quad (2.25)$$

$$\frac{\mathcal{E}_{\text{junc}}^{n+1} - \mathcal{E}_{\text{junc}}^n}{\Delta t} = (\lambda_{123}^{n+1/2})^* \bar{p}_{123}^{n+1/2}. \quad (2.26)$$

Therefore the numerical scheme for junctions stores energy in γ and redistributes it in the pipes, without any loss.

2.2.4 Schur complement

The final goal is to find the explicit computations that must be done for updating the variables. As in the case of radiation, we express $E_i^* \mu P_i^{n+1/2}$ in terms of what we need to calculate (in this case γ):

$$\bar{p}_{123}^{n+1/2} = p_{\text{no flow } 123}^{n+1/2} - \frac{\Delta t}{2} m_{\text{end } 123}^{-1} \lambda_{123}^{n+1/2}, \quad \lambda_{123}^{n+1/2} = -T_J^* \bar{\gamma}^{n+1/2},$$

where $p_{\text{no flow } 123}^{n+1/2}$ is the vector of the three $p_{\text{no flow}}^{n+1/2}$ defined by equation (2.3), and $m_{\text{end } 123}$ is the 3×3 diagonal matrix of end masses:

$$m_{\text{end } 123} = \begin{pmatrix} m_{\text{end } 1} & 0 & 0 \\ 0 & m_{\text{end } 2} & 0 \\ 0 & 0 & m_{\text{end } 3} \end{pmatrix}, \quad p_{\text{no flow } 123}^{n+1/2} = \begin{pmatrix} p_{\text{no flow } 1}^{n+1/2} \\ p_{\text{no flow } 2}^{n+1/2} \\ p_{\text{no flow } 3}^{n+1/2} \end{pmatrix}.$$

Simple operations give us the following expressions for γ^{n+1} and $\lambda^{n+1/2}$:

$$\begin{aligned} M_{J\Delta t} &:= M_J + \frac{\Delta t^2}{4} T_J m_{\text{end } 123}^{-1} T_J^*, \\ \bar{\gamma}^{n+1/2} &= M_{J\Delta t}^{-1} \left(M_J \gamma^n - \frac{\Delta t}{2} T_J p_{\text{no flow } 123}^{n+1/2} \right), \quad \gamma^{n+1} = 2\bar{\gamma} - \gamma^n, \\ \lambda^{n+1/2} &= -T_J^* \bar{\gamma}^{n+1/2}. \end{aligned}$$

Note that matrix $M_{J\Delta t}$ is 2×2 , so its inversion has negligible computational cost. As in the case of radiation, it is possible to limit the number of operations by calculating in advance all constant factors.

2.3 Reed model

Apart from resonance in the tube, the most important part of an instrument is its source of vibration. Many researchers study the production of sound

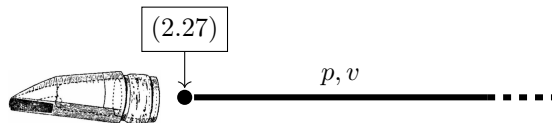


Figure 2.6: Reed model at the end of a pipe

by various source elements, starting with Helmholtz who gave early models of inward-striking and outward-striking reeds [30]. One great challenge arises from the number of parameters which the musician can modify in real-time, rendering quantitative experiments with musicians very difficult. Some researchers have used artificial mouths [15, 19, 31] to ensure precise control, while others perform measurement on actual musicians in search for accurate models and playing parameters [14, 22].

The focus is here on reed models, because of their versatility in representing all at once single reeds, double reeds, and the so-called “lip-reeds” (lips of brass players). Indeed, all these act as a kind of valve, modulating the amount of air flowing from one side to the other, while at the same time being controlled by the pressure difference between the player’s mouth and the mouthpiece or bocal. As a consequence, the basic models for all these elements concur [12].

We use a reed model with a single degree of freedom y representing the reed opening, inspired by the literature on clarinet reeds [7, 23, 35, 48]:

$$\ddot{y} + g\dot{y} + \omega_0^2(y - y_0) - \frac{\omega_1^\alpha}{y_0^{\alpha-1}}|y^-|^{\alpha-1} = -\frac{S_r \Delta p}{m_r}, \quad (2.27)$$

where g is a damping factor, ω_0 , ω_1 are natural frequencies of the reed, y_0 is the opening at rest, S_r and m_r model respectively a characteristic surface and characteristic mass of the reed, and $\Delta p = p_m - p(0, t)$ is the pressure difference between the mouth and the beginning of the instrument bore. The mouth pressure p_m may be time-varying. The notations y^+ , y^- are used for the positive part and the negative part of y , namely $y^+ = \frac{1}{2}(y + |y|)$ and $y^- = \frac{1}{2}(y - |y|)$. The nonlinear term activates for negative y , when the reed hits the facing curve of the mouthpiece. Its power α is determined empirically.

We put this model under the more generic form

$$m_r(\ddot{y} + g\dot{y}) + F'(y) = -S_r \Delta p, \quad (2.28)$$

where F is a potential energy associated to the reed’s elasticity, namely:

$$F(y) = m_r \left[\frac{\omega_0^2}{2}(y - y_0)^2 + \frac{\omega_1^\alpha}{\alpha y_0^{\alpha-1}}|y^-|^\alpha \right]. \quad (2.29)$$

The flow entering the instrument’s chamber is then given by applying a Bernoulli law. We compensate this flow with the chamber size variation caused by the motion of the reed.

$$v(0, t) = w y^+ \sqrt{\frac{2|\Delta p|}{\rho}} \text{sign}(\Delta p) - S_r \dot{y} \quad (2.30)$$

Following our convention, we use a Lagrange multiplier λ corresponding to $-v(0, t)$, in addition to the reed's position y and velocity \dot{y} .

$$\begin{cases} \Delta p = p_m - p(0, t) \\ m_r(\ddot{y} + g\dot{y}) + F'(y) + S_r\Delta p = 0 \\ \lambda + wy^+ \sqrt{\frac{2|\Delta p|}{\rho}} \operatorname{sign}(\Delta p) - S_r\dot{y} = 0, \end{cases} \quad (2.31)$$

The energy balance of this system is:

$$\begin{cases} \frac{m_r}{2} \frac{d}{dt}(\dot{y}^2) + m_r g \dot{y}^2 + \frac{d}{dt}F(y) + S_r \dot{y} \Delta p = 0 \\ \lambda p_m - \lambda p(0, t) + wy^+ \sqrt{\frac{2|\Delta p|}{\rho}} |\Delta p| - S_r \dot{y} \Delta p = 0. \end{cases} \quad (2.32)$$

Different terms are in conservative form:

$$\mathcal{E}_{\text{reed}} := F(y) + \frac{m_r}{2} \dot{y}^2,$$

and the sum of these equations gives the energy balance of the reed:

$$\frac{d}{dt} \mathcal{E}_{\text{reed}} = -W_{\text{reed}} + S_{\text{musician}} - Q_{\text{reed}}, \quad (2.33)$$

where we distinguish the work of the reed on the pipe, the source term from the musician blowing, and the losses $Q_{\text{reed}} \geq 0$:

$$\begin{aligned} W_{\text{reed}} &= -\lambda p(0, t), \\ S_{\text{musician}} &= -\lambda p_m, \\ Q_{\text{reed}} &= m_r g \dot{y}^2 + wy^+ \sqrt{\frac{2}{\rho}} |\Delta p|^{3/2}. \end{aligned}$$

Several terms appear in the losses, including both the energy dissipated due to mechanical damping of the reed, and the energy lost due to turbulent mixing of the thin air jet entering the chamber.

Note that when there is no pressure source, $p_m = 0$ (player not blowing), the source term is zero, and so the energy is non-increasing.

Explicit scheme without contact

We focus on the special case where nonlinearity is only due to the Bernoulli law.

When we neglect the influence of contact between the reed and the mouthpiece by setting $\omega_1 = 0$, the reed acts as a forced damped linear spring. Note that the formula for the flow remains nonlinear. We also introduce an additional variable z corresponding to \dot{y} . In order to preserve an energy, we write a

first-order scheme, similar to that used for the pipe:

$$\begin{cases} \Delta p^{n+1/2} = p_m^{n+1/2} - E^* \mu P^{n+1/2}, \\ m_r \left(\frac{z^{n+1} - z^n}{\Delta t} + g \bar{z}^{n+1/2} \right) + m_r \omega_0^2 (y^{n+1/2} - y_0) + S_r \Delta p^{n+1/2} = 0, \\ \frac{y^{n+1/2} - y^{n-1/2}}{\Delta t} - z^n = 0, \\ \lambda^{n+1/2} = w(y^{n+1/2}) + \sqrt{\frac{2|\Delta p^{n+1/2}|}{\rho}} \text{sign}(\Delta p^{n+1/2}) + S_r \bar{z}^{n+1/2}. \end{cases} \quad (2.34)$$

Conservation of energy

Let us find the discrete counterpart of energy equation (2.33). For ease of notation, we will simply write \bar{z} for $\bar{z}^{n+1/2}$, and μP for $\mu P^{n+1/2}$. From the system (2.34) we deduce:

$$\begin{cases} \bar{z} m_r \frac{z^{n+1} - z^n}{\Delta t} + m_r g \bar{z}^2 + m_r \omega_0^2 \bar{z} (y^{n+1/2} - y_0) + S_r \bar{z} \Delta p^{n+1/2} = 0 \\ m_r \omega_0^2 (y^{n+1/2} - y_0) \left[\frac{\bar{y}^{n+1} - \bar{y}^n}{\Delta t} - \bar{z} \right] = 0 \\ \lambda^{n+1/2} (p_m^{n+1/2} - E^* \mu P) + w(y^{n+1/2}) + \sqrt{\frac{2}{\rho}} \left| \Delta p^{n+1/2} \right|^{3/2} - S_r \bar{z} \Delta p^{n+1/2} = 0. \end{cases} \quad (2.35)$$

We simplify these equations into:

$$\begin{cases} \frac{\mathcal{E}_z^{n+1} - \mathcal{E}_z^n}{\Delta t} + m_r g \bar{z}^2 + m_r \omega_0^2 \bar{z} (y^{n+1/2} - y_0) + S_r \bar{z} \Delta p^{n+1/2} = 0 \\ \frac{\mathcal{E}_y^{n+1} - \mathcal{E}_y^n}{\Delta t} - m_r \omega_0^2 \bar{z} (y^{n+1/2} - y_0) = 0 \\ \lambda^{n+1/2} p_m^{n+1/2} - \lambda^{n+1/2} E^* \mu P + w(y^{n+1/2}) + \sqrt{\frac{2}{\rho}} \left| \Delta p^{n+1/2} \right|^{3/2} - S_r \bar{z} \Delta p^{n+1/2} = 0. \end{cases} \quad (2.36)$$

where we have defined the energies:

$$\begin{aligned} \mathcal{E}_z^n &= \frac{1}{2} m_r (z^n)^2 \\ \mathcal{E}_y^n &= \frac{1}{2} m_r \omega_0^2 (y^{n+1/2} - y_0)(y^{n-1/2} - y_0) \\ \mathcal{E}_{\text{reed}}^n &= \mathcal{E}_y^n + \mathcal{E}_z^n \end{aligned}$$

The sum of all the equations of (2.36) gives a discrete energy conservation result similar to (2.33):

$$\frac{\mathcal{E}_{\text{reed}}^{n+1} - \mathcal{E}_{\text{reed}}^n}{\Delta t} = -W_{\text{reed}}^{n+1/2} + S_{\text{musician}}^{n+1/2} + Q_{\text{reed}}^{n+1/2}. \quad (2.37)$$

A discrete version of the same terms as before appear in the energy balance equation. The dissipation terms are still guaranteed to be negative.

$$\begin{aligned} W_{\text{reed}}^{n+1/2} &= -\lambda^{n+1/2} E^* \mu P^{n+1/2} \\ S_{\text{musician}}^{n+1/2} &= -\lambda^{n+1/2} p_m^{n+1/2} \\ Q_{\text{reed}}^{n+1/2} &= m_r g (\bar{z}^{n+1/2})^2 + w(y^{n+1/2})^+ \sqrt{\frac{2}{\rho}} |\Delta p^{n+1/2}|^{3/2}. \end{aligned}$$

Note how \mathcal{E}_y^n depends on two different time steps $n - 1/2$ and $n + 1/2$. To ensure positivity of the energy, we need to reformulate it. As in equation (1.32), a stability condition will naturally emerge. Expressing $y^{n+1/2}$ and $y^{n-1/2}$ in terms of \bar{y}^n and z^n allows us to write:

$$\mathcal{E}_y^n + \mathcal{E}_z^n = \frac{1}{2} \left[m_r \omega_0^2 (\bar{y}^n - y_0)^2 + m_r \left(1 - \frac{\Delta t^2}{4} \omega_0^2 \right) (z^n)^2 \right]. \quad (2.38)$$

For the energy to be positive, one must have $1 - \frac{\Delta t^2}{4} \omega_0^2 > 0$, which is equivalent to:

$$\Delta t < \frac{2}{\omega_0}. \quad (2.39)$$

This conditions the stability of the reed's numerical scheme.

Remark. *It is possible to devise another scheme, inspired from the so-called θ -schemes [10], with unconditional stability. However, seeing that the stability condition given above is not too restrictive in most cases, I did not take the time to study that other scheme.*

Making the scheme explicit

System (2.34) does not allow to compute the scheme stepwise directly. There is mutual dependence between P^{n+1} and z^{n+1} through $\lambda^{n+1/2}$. We need to reduce this to a single nonlinear equation, which happens to be exactly solvable. Let us repeat their equations in terms of μP and \bar{z} .

$$\begin{cases} 2M^{H^1} \frac{\mu P - P^n}{\Delta t} + B^* V^{n+1/2} - \lambda^{n+1/2} E = 0 \\ \Delta p^{n+1/2} = p_m^{n+1/2} - E^* \mu P^{n+1/2} \\ 2m_r \frac{\bar{z} - z^n}{\Delta t} + m_r g \bar{z} + m_r \omega_0^2 (y^{n+1/2} - y_0) + S_r \Delta p^{n+1/2} = 0 \\ -\lambda^{n+1/2} + w(y^{n+1/2})^+ \sqrt{\frac{2|\Delta p^{n+1/2}|}{\rho}} \text{sign}(\Delta p^{n+1/2}) - S_r \bar{z} = 0. \end{cases}$$

We reverse equation (2.2) to find the affine dependence of $\lambda^{n+1/2}$ on $E^* \mu P$:

$$\begin{aligned} \lambda^{n+1/2} &= a_{\lambda 0} E^* \mu P + b_{\lambda 0}, \\ \text{where } a_{\lambda 0} &= -\frac{2m_{\text{end}}}{\Delta t} \\ \text{and } b_{\lambda 0} &= \frac{2m_{\text{end}}}{\Delta t} p_{\text{no flow}}^{n+1/2}. \end{aligned}$$

Since moreover $E^* \mu P = p_m^{n+1} - \Delta p^{n+1/2}$, a relation between λ and Δp follows:

$$\lambda^{n+1/2} = a_\lambda \Delta p^{n+1/2} + b_\lambda, \quad (2.40)$$

where $a_\lambda = -a_{\lambda 0}$ and $b_\lambda = a_{\lambda 0} p_m^{n+1/2} + b_{\lambda 0}$:

$$a_\lambda = \frac{2m_{\text{end}}}{\Delta t}, \quad b_\lambda = \frac{2m_{\text{end}}}{\Delta t} (p_{\text{no flow}}^{n+1/2} - p_m^{n+1/2}).$$

Similarly, $\bar{z}^{n+1/2}$ follows an affine relation with $\Delta p^{n+1/2}$:

$$\bar{z}^{n+1/2} = a_{\bar{z}} \Delta p^{n+1/2} + b_{\bar{z}}, \quad (2.41)$$

where

$$a_{\bar{z}} = -\frac{S_r \Delta t}{m_r(2 + g\Delta t)}, \quad \text{and } b_{\bar{z}} = \frac{z^n - \frac{\Delta t}{2} \omega_0^2 (y^{n+1/2} - y_0)}{1 + g \frac{\Delta t}{2}}.$$

This allows us to transform the nonlinear equation into:

$$\alpha \Delta p + \gamma \sqrt{|\Delta p|} \text{sign}(\Delta p) + \beta = 0$$

where

$$\begin{aligned} \alpha &= a_\lambda - S_r a_{\bar{z}}, \\ \beta &= b_\lambda - S_r b_{\bar{z}}, \\ \gamma &= w(y^{n+1/2})^+ \sqrt{2/\rho}. \end{aligned}$$

Specifically in this case, $\alpha = \frac{m_{\text{end}}}{2\Delta t} + \frac{S_r^2 \Delta t}{m_r(2+g\Delta t)}$ is positive, and γ is nonnegative.

- When $\gamma = 0$, the nonlinear term vanishes and the solution is directly:

$$\Delta p = -\beta/\alpha \quad (2.42)$$

- When γ is strictly positive, we set $q = \sqrt{|\Delta p|}$, and use $\sigma = \pm 1$ as an unknown for the sign: $\sigma = \text{sign}(\Delta p)$. The equation is then

$$\alpha q^2 + \gamma q + \sigma \beta = 0.$$

Its determinant is $\Delta = \gamma^2 - 4\sigma\alpha\beta$, and the associated roots are

$$q_{\pm} = \frac{-\gamma \pm \sqrt{\gamma^2 - 4\sigma\alpha\beta}}{2\alpha}.$$

The solutions are valid only if $q \geq 0$. Since both α and γ are positive, q_- is negative and cannot be a solution. For q_+ to be nonnegative, $\sqrt{\Delta}$ must be larger than γ , and so we must have $\sigma = -\text{sign}(\beta)$. Therefore the only solution is:

$$\Delta p = -\text{sign}(\beta) \left(\frac{-\gamma + \sqrt{\gamma^2 + 4\alpha|\beta|}}{2\alpha} \right)^2. \quad (2.43)$$

From here, it is possible to compute directly $\lambda^{n+1/2}$ and $\bar{z}^{n+1/2}$ through their affine dependence in Δp , given by equations (2.40) and (2.41).

Remark. *The assumption $\omega_1 = 0$ allows to write an explicit scheme. If we were to take into account the mechanical nonlinearity of the reed, an implicit scheme would be necessary. Using an iterative procedure would allow to solve the system approximately at each step. I did not take the time to implement such a scheme during my internship.*

Chapter 3

Implementation

The numerical schemes presented in chapters 1 and 2 were implemented in Python 3 using object-oriented programming, as part of the OpenWIND toolbox. This toolbox is aimed at making the state-of-the-art methods in musical acoustics available and readily usable, for researchers and also for instrument makers.

3.1 Sectioning of the toolbox

During the time of my internship, the toolbox was brought to critically change, as its old conformation prevented the integration of new elements, such as time-domain simulation or inverse problems.

I first coded the schemes while at the same time I was studying and discovering them. In the early scripts, everything worked together: there was a single scheme involving pipes, radiation, and a reed model at the same time. But I soon realized that different elements could be separated, and would only interact through boundary variables—those variables are called $\lambda^{n+1/2}$ throughout this document. Such a sectioning of the schemes has several benefits:

- Arbitrarily complex instruments can be assembled.
- Any of the implemented schemes can be combined together. For instance, switching between lossless and lossy pipes is trivial.
- New energy-consistent models can easily be added later on, and used alongside the already-existing.
- The little amount of communication required between the elements would allow the computation to be largely parallelized, if we were using a language that supports efficient multi-threading.

Each pipe is thus represented as an object, and so is every radiating part, every junction, and the reed model. These choices are reflected in the structure of the toolbox, for which a tentative UML diagram is shown in figure 3.1.

3.2 Scheme convergence

We test the convergence of the numerical schemes on a few simple test cases.

3.2.1 L^2 norm

We simulate a simple lossless cylinder of length 20 cm and radius 8 mm, closed at the right end ($\lambda_{(+)} = 0$), in which a smooth impulse $\lambda_{(-)}(t)$ is sent. The impulse lasts 4 ms, and the simulation is performed for a total duration of 20 ms. The discretization is performed for a range of element lengths and orders. Each different discretization gives another value of time step Δt , chosen according to condition (1.32). For each simulation, the pressure field is interpolated in x with the use of basis functions ϕ_k , and linearly interpolated in time, in order to compare with the reference (converged) result at the same points in space and time.

Results are shown in figure 3.2. We see that, regardless of the order of the elements, the resulting error evolves as the square of the element length. The reason is that the space-time convergence of the scheme is only guaranteed to be in $\mathcal{O}(\Delta t^2)$ [26]. Since the time step is chosen as

$$\Delta t = \alpha \Delta t_{max} \quad \Delta t_{max} = 2 \left[\rho \left((M^{H^1})^{-1} B^* M^{L^2} B \right) \right]^{-\frac{1}{2}},$$

with α a constant close to 1¹, the resulting error is mainly due to the time integration, and not to the spatial discretization.

3.2.2 Point-wise convergence

As we are mainly interested in the sound produced by the instrument, the important data are at the ends of the instrument. Luckily, if instead of considering the L^2 norm of the difference, we consider the pointwise error, for instance at the mouth-end, it also converges at order 2, as shown in figure 3.3.

3.2.3 Radiation

We now add a radiating boundary condition at the end of the cylindrical instrument, as described in section 2.1.3. The toolbox automatically calculates radiation coefficients according to formulas from the literature [12]. The signal is observed at point $x = 0$. Figure 3.4 shows that the error still evolves at order two with respect to the element length.

3.2.4 Junction

We add a hole at 5 cm from the mouth, of radius 3 mm and length 3 cm. The scheme makes use of the three-way junction described in section 2.2. The pointwise error on p is observed at the mouth-end, in figure 3.4.

3.2.5 Reed model

Instead of sending a fixed pulse $\lambda(t)$ into the instrument, we add a reed model, with parameters chosen to correspond more or less to a bassoon reed. The obtained convergence is shown in figure 3.5.

¹In our examples, we always use $\alpha = 1$ unless specified otherwise. Although our proof of stability does not hold in this case, it can be shown to pose no problem [10].

It exhibits a convergence at order lower than 2, which is unsatisfactory when compared to the other schemes. This may be due to the non-smooth behavior of the reed around $y = 0$, or to issues in the implementation. Future work should be dedicated to a better numerical scheme, with theoretical error analysis.

3.2.6 Viscothermal losses

Taking the cylinder with one hole, we now add viscothermal losses to all pipes. The resulting error convergence is shown in figure 3.4. In spite of the important complexity of the new scheme, it has no problem converging, at order two as a function of the element length. It even results in a slightly smaller error than the lossless scheme, probably due to the faster damping of problematic high frequencies.

3.2.7 A complex instrument: the bassoon

The team developing OpenWIND works jointly with a bassoon maker, Augustin Humeau. Over the span of about 20 years, he refined his manufacturing process for baroque bassoons. Given a numerical model of his bassoon, our schemes allow to simulate the propagation of acoustic waves in the instrument. Moreover, the reed model enables the computation of bassoon sounds, as if played by an artificial mouth (i.e. with no random fluctuation of pressure or control parameters).

The baroque bassoon is an approximately conical instrument, with twelve tone holes placed along its length which may be opened or closed during play. A numerical model of the bassoon was obtained from technical drafts by Augustin Humeau.

We simulate its impulse response at a fixed discretization level, adapted so that the error at all frequencies from the hearing range of humans (20 Hz to 20 000 Hz) is small. We progressively refine the time step Δt to observe the rate of convergence of the temporal scheme. At the CFL, the relative error is already only 1.3×10^{-5} ; but it decreases at order 2 when the time step is reduced. Note that, thanks to the precision of the spectral finite elements, the error due to the discretization is negligible compared to the error introduced by the time-domain scheme.

3.3 Energy conservation

The numerical schemes described in chapters 1 and 2 are guaranteed to preserve a numerical energy. In the toolbox, each object can compute its own energy; it is thus easy to check that the energy is globally preserved (or dissipated in the corresponding case), independently of the spatial or temporal discretization.

3.3.1 Simple case: the cylindrical instrument

We send a smooth 1 ms pulse into the example cylinder with one hole described above, and we observe the amount of energy in the different pipes, in the junction, and in the two radiating elements (end of the instrument, and end of the hole). We also compute the amount of energy lost to radiation according to equation (2.17). The exchanges of energy are shown in figure 3.7a.

Additionally, we compute the variation of energy due to numerical noise:

$$\varepsilon^{n+1/2} = \frac{\mathcal{E}^{n+1} - \mathcal{E}^n}{\Delta t} + Q^{n+1/2}. \quad (3.1)$$

The values of $\varepsilon^{n+1/2}$ are shown in figure 3.7b. Computing time is a few seconds on a

The same computations are performed with viscothermal losses: results are in figure 3.8.

3.3.2 The bassoon

The same short pulse is sent into the bassoon model. The results are shown in figures 3.9 and 3.10.

3.4 Sound synthesis

The orifices of wind instruments radiate sound into the open air. The resulting sound, as heard by a listener placed some distance away from the instrument, is related to the pressure in front of the openings, by several effects:

- The propagation of sound results in a small delay, and a reduction of the amplitude of the signal according to the inverse square law.
- Directivity of each opening may filter the output. This effect is relatively weak for woodwinds, whose openings are small compared to the typical wavelength of playing; but is much more significant in brass. For example, a trumpet bell will radiate high frequencies in a very directional manner², so that two listeners placed in front or behind the player will hear dramatically different sounds, not only in terms of volumes, but also of timbre [38].
- In the case of woodwinds, the superposition of waves coming from different tone holes can result in complex directivity patterns [4, 21, 39].
- Reverberation in the room can blend all these outputs in varied ways, and is commonly known to be critical to the perception of music.

For simplicity, all these effects were simply ignored in a first approach. A single virtual microphone was set to record the value of the pressure at the bell of the instrument. The signals obtained were anti-aliased and resampled at 44.1 kHz to produce sound files.

The impulse response of a cylinder is shown in figure 3.11. The simulations took a few minutes to run on a standard recent laptop. We can see the influence of the open end of a tube on radiation, and also how viscothermal effects shorten the sound.

A simulation of a bassoon played with a reed is shown in figure 3.12. The simulation runs in about 6 minutes on a laptop for one second of sound. After a short attack transient, a periodic regime is attained. The frequency is not exactly the one expected, probably due to the choice of reed parameters.

²A fact well-known by musicians who were ever placed in front of the trumpets in a band or orchestra.

Description des données / Classes

Toutes les classes ci-dessous permettent de construire les instruments, dans l'objectif de faire des calculs dans le domaine fréquentiel et des simulations temporelles

Chefs d'orchestre: Construction d'instruments, calculs fréquentiels, simulations temporelles

Toutes les classes ci-dessous créent les différents graphes représentant l'instrument ainsi que ses interactions selon la fonctionnalité visée. Elles implémentent aussi les fonctionnalités d'OpenWind (calcul d'impédance, simulations temporelles).

légende:
 → est associé à
 → est hérité de
 → est implémenté
 → compose / est une partie de

listes de positions et de rayons pour la forme intérieure de la géométrie et l'information sur chacun des trous

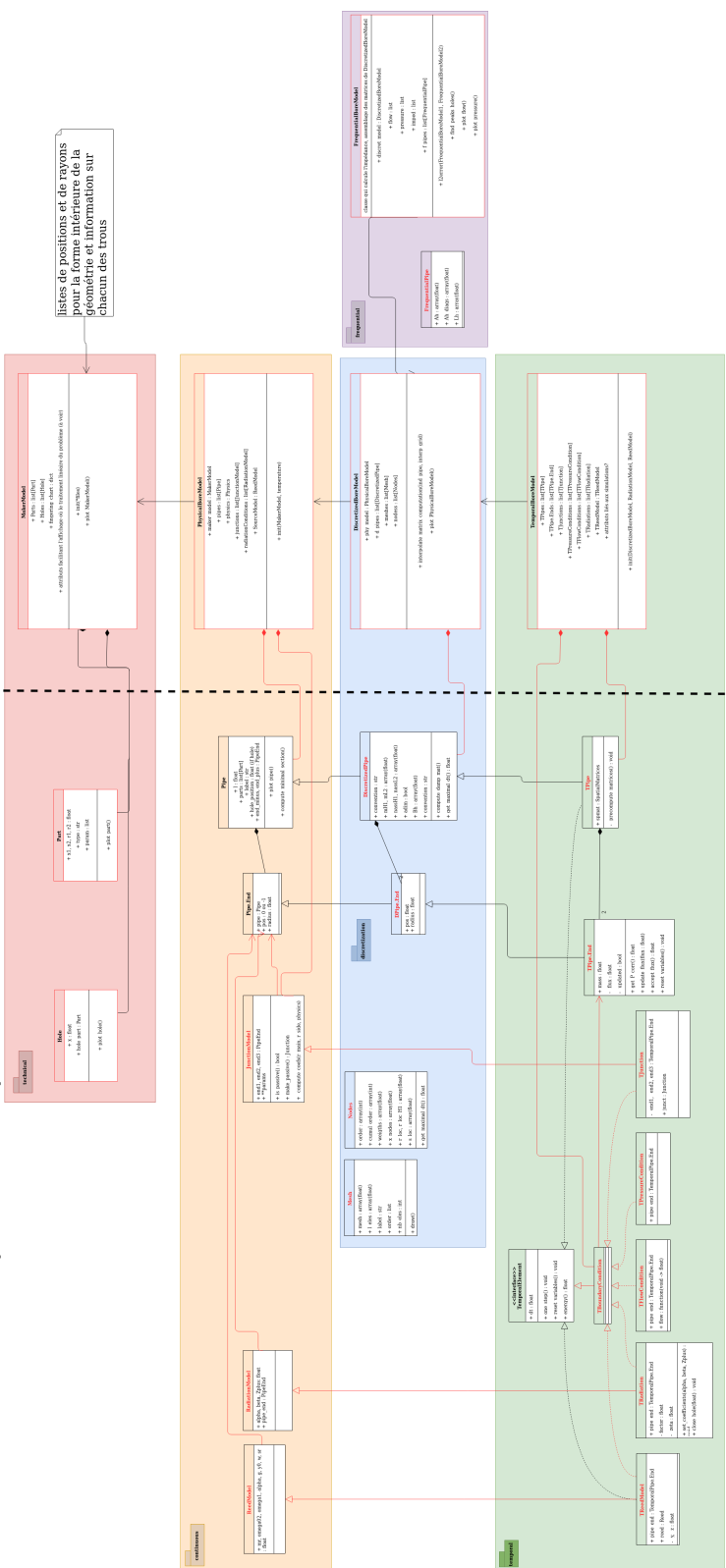


Figure 3.1: The planned UML diagram of OpenWind. Each box denotes a class, and each colored block is a module. The toolbox has evolved since, and does not strictly follow it.

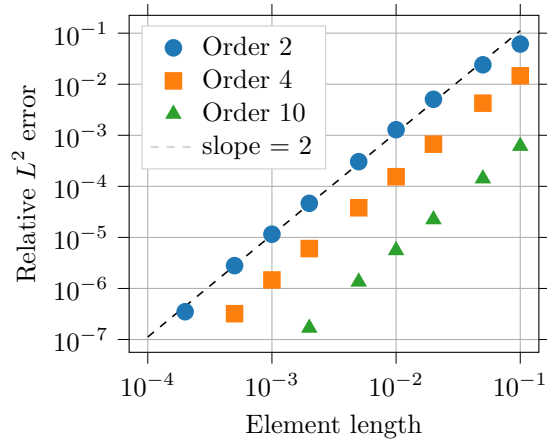


Figure 3.2: Largest relative error $\frac{\sup_t \|p_i(t) - p(t)\|_{L^2}}{\sup_t \|p(t)\|_{L^2}}$, for various element lengths and orders.

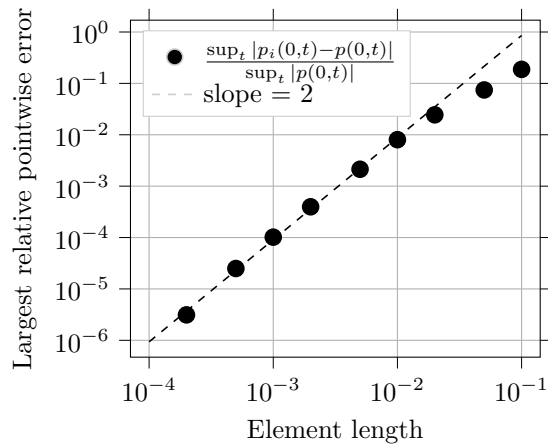


Figure 3.3: Cylinder, closed at both ends. Largest relative pointwise error at the mouth-end during the simulation, for various element lengths. Basis functions on each element are of order 2.

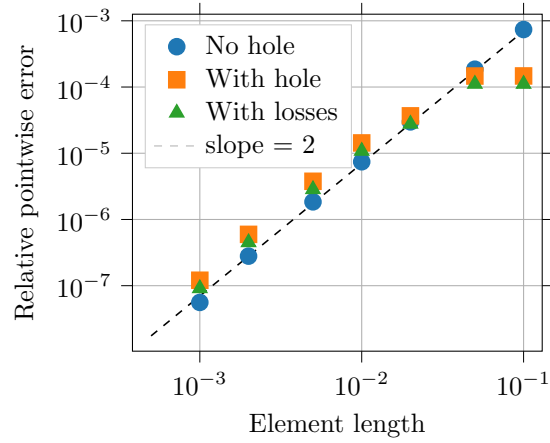


Figure 3.4: Cylinder with radiation condition, cylinder with one hole, and finally with viscothermal losses. Largest relative pointwise error during the simulation, as a function of the element length. Basis functions on each element are of order 10.

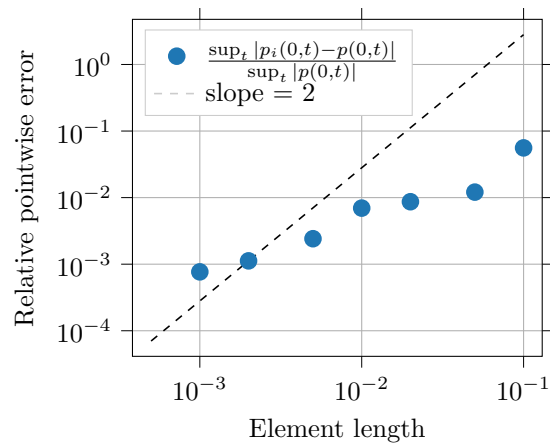


Figure 3.5: One-hole cylinder with a reed. The scheme converges, although at a lower order than expected. Basis functions on each element are of order 10.

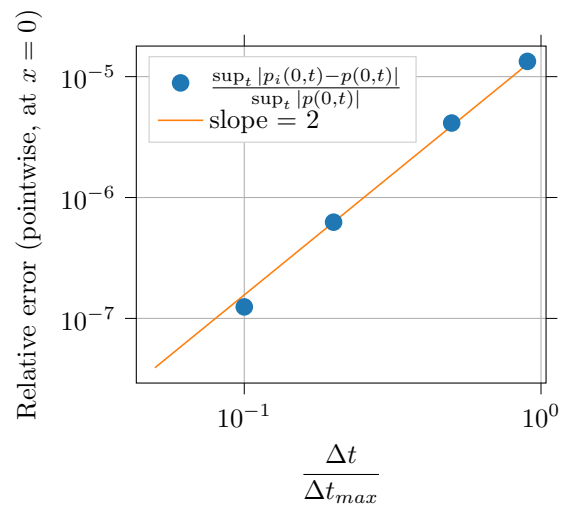
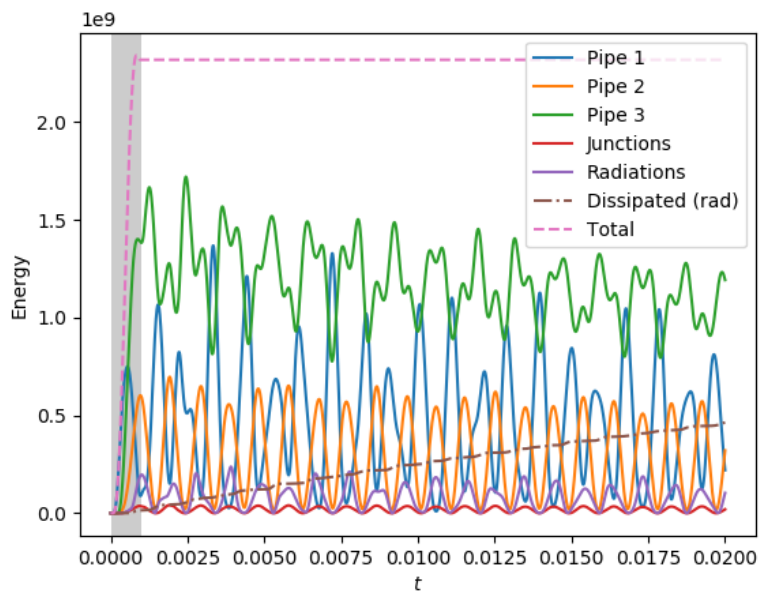
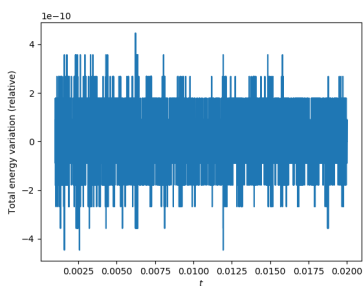


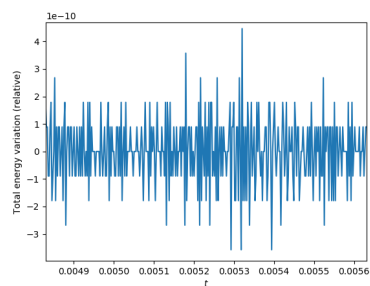
Figure 3.6: Baroque bassoon, with 12 junctions, 13 radiation conditions, and 25 lossy pipes, excited by a pulse. The scheme converges at order 2 in Δt . Basis functions on each element are of order 4, and the instrument is discretized into elements of 5 mm or shorter.



(a) Energy exchanges. Initial impulse lasts 1 ms (grayed zone).

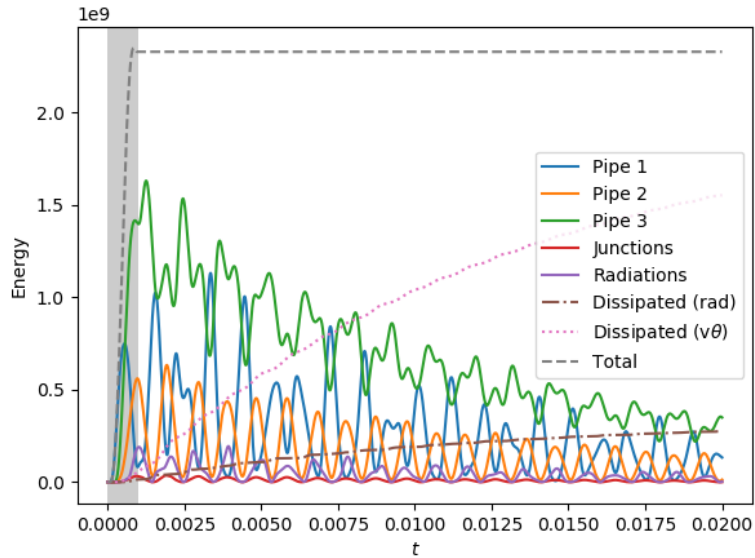


(b) Numerical error on the energy.

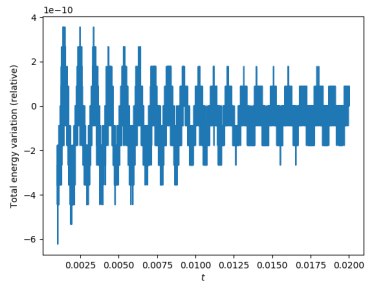


(c) Detail of previous.

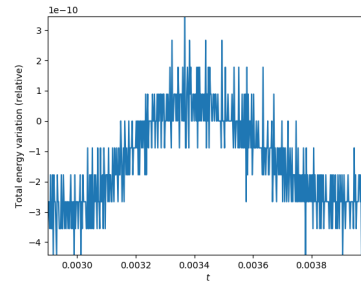
Figure 3.7: Cylinder with one hole, without viscothermal losses. Note the quantization of error due to floating-point rounding.



(a) Energy exchanges. Initial impulse lasts 1 ms (grayed zone).

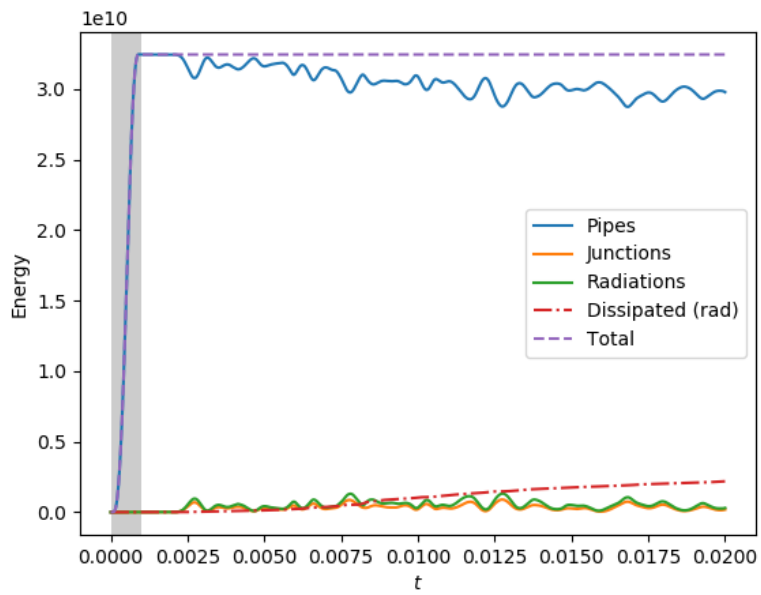


(b) Numerical error on the energy.

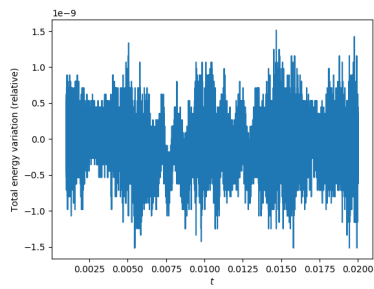


(c) Detail of previous.

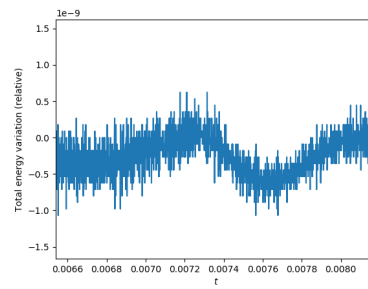
Figure 3.8: Cylinder with one hole, with viscothermal losses. Note that most of the energy dissipation is due to viscothermal losses, which contribute more than 5 times as much as radiation in this case. Also note that the error is still quantized, but that it has a slight bias during oscillations of the pipe. This may be due to implementation details of the scheme with losses.



(a) Energy exchanges. Initial impulse lasts 1 ms (grayed zone).

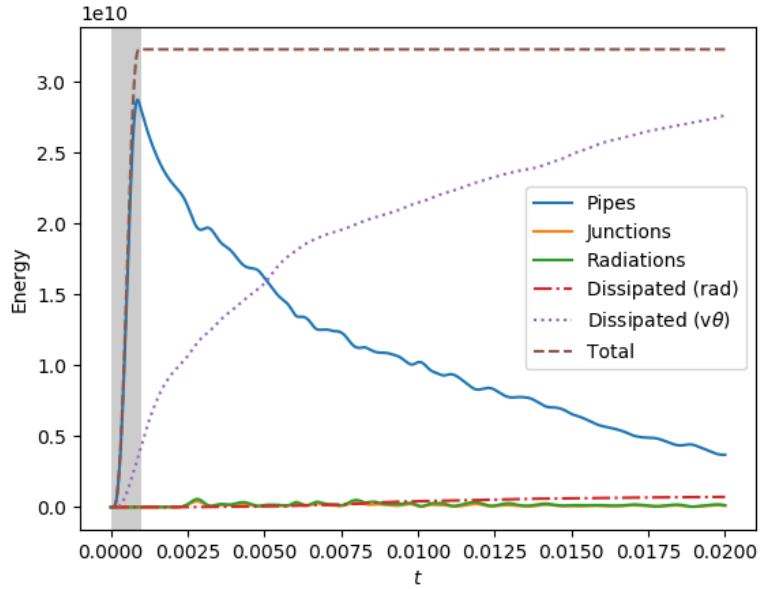


(b) Numerical error on the energy.

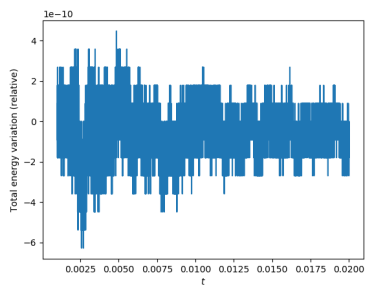


(c) Numerical error exhibits some trends.

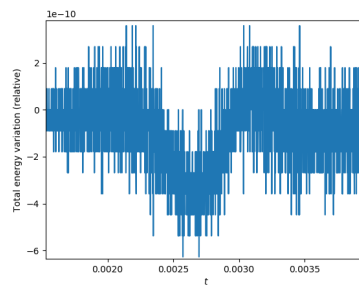
Figure 3.9: Bassoon, without viscothermal losses.



(a) Energy exchanges. Initial impulse lasts 1 ms (grayed zone). We observe the crucial importance of the dissipation due to the viscous and thermal effects, with under 3% of the initial energy input being converted to audible sound. This preeminence of losses is due to the small radius of the bassoon crook (about 2 mm at the mouth-end) and also to the fact that the impulse contains many high frequencies, which are more strongly damped.

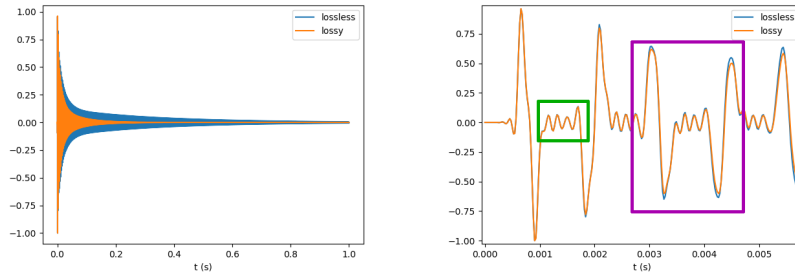


(b) Numerical error on the energy.



(c) Detail of previous.

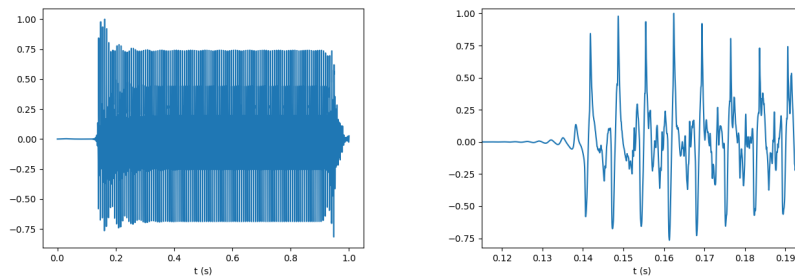
Figure 3.10: Bassoon, with viscothermal losses.



(a) Whole simulation. We see clearly the quicker dampening of the signal due to viscothermal losses.

(b) First few milliseconds. The signal initially echoes the impulse, which is reflected between the two ends of the pipe with one change of sign on each round trip (purple). It quickly disperses (green) after reaching the radiating end, and becomes progressively smoother due to radiation and losses.

Figure 3.11: Impulse response of a radiating cylinder, with and without viscothermal losses.



(a) Whole simulation. The pressure in the player's mouth p_m is varied during the simulation, with a smooth increase and decrease.

(b) The scheme simulates realistic attack transients.

Figure 3.12: Simulation of a baroque bassoon playing a medium F (fourth line of the bass key).

Conclusion and perspectives

The study of wind instruments is a multifaceted topic. They consist of compound systems, in which a large range of physical phenomena are entangled, some of which not yet well understood, involving non-linear behaviors and coupling between solids and fluids.

We presented here a set of models for simulating various parts of a wind instrument under a common formalism, allowing the combined use of the results of long-standing research in music acoustics.

Some perspectives of development are:

- Comparison with real data: although our algorithms converge to solutions of the model equations with a very high precision, experimental insight would be required to ensure the validity of the results.
- Improving junction models: as seen in section 2.2, the usual writing for junction models in frequency domain makes use of negative masses, which are problematic in the time domain.
- Studying the radiation of a tone hole: when a finger or pad is partially blocking the opening, we do not know what coefficients to use in our model (2.7). The impedance at the end of a pipe could also follow more complicated laws.
- Adapting hydrodynamic jet models, especially the “jet-drive” model [12] to be able to simulate flute-like instruments. This model poses some problems in the time domain.
- Spherical/curvilinear [28]/multi-mode propagation in the pipes: the plane-wave assumption is problematic for instruments with quickly-varying section; better models are required for faithful simulation of brass instrument bells.
- Non-linear losses have been shown to occur in small tone holes due to viscous effects, with significant influence on playability in the clarinet [1].
- Optimization of control parameters: a major topic in music acoustics which we did not cover here is, how to set the embouchure and blowing parameters in order to obtain the intended sound [17, 20]? Musicians require years of training for this task; maybe a computer could find good answers, but objective criteria need to be established.
- Vocal tract simulation: the vocal tract is an acoustic resonator with a shape that may vary in time (as words are articulated, for instance) [32].

It also influences the playing of some musical instruments such as the didjeridoo, or even the saxophone in altissimo register [13, 49]. Taking it into account could prove valuable.

Another main objective of OpenWIND is to perform reconstruction of an instrument bore, given some expected characteristics. Work is ongoing on this topic, which also requires finding suitable criteria for the numerical optimization [34, 50].

All these ideas will require joint effort between acousticians and mathematicians, with work needed in experimentation, in numerical simulation, in modeling, and in analysis. I will begin to uncover a few of these possibilities during a follow-up to my internship, from September 2019 to February 2020.

Bibliography

- [1] Mérouane Atig, Jean-Pierre Dalmont, and Joël Gilbert. Saturation mechanism in clarinet-like instruments, the effect of the localised non-linear losses. *Applied Acoustics*, 65(12):1133–1154, 2004.
- [2] Ivo Babuska, OC Zienkiewicz, J Gago, and ER de A Oliveira. *Accuracy estimates and adaptive refinements in finite element computations*. John Wiley & Sons New York, 1986.
- [3] Hélène Barucq, Juliette Chabassier, Marc Duruflé, Laurent Gizon, and Michael Leguèbe. Atmospheric radiation boundary conditions for the helmholtz equation. *ESAIM: Mathematical Modelling and Numerical Analysis*, 52(3):945–964, 2018.
- [4] Arthur H Benade. On the mathematical theory of woodwind finger holes. *The Journal of the Acoustical Society of America*, 32(12):1591–1608, 1960.
- [5] Kenneth W Berger. Some factors in the recognition of timbre. *The Journal of the Acoustical Society of America*, 36(10):1888–1891, 1964.
- [6] Harold Benjamin, Bruno Lombard, Christophe Vergez, and Emmanuel Cotanceau. Time-domain numerical modeling of brass instruments including nonlinear wave propagation, viscothermal losses, and lips vibration. *Acta Acustica united with Acustica*, 103(1):117–131, 2017.
- [7] Stefan Bilbao. Direct simulation for wind instrument synthesis. In *Conference on Digital Audio Effects*, pages 145–152, 2008.
- [8] Stefan Bilbao and Reginald Harrison. Passive time-domain numerical models of viscothermal wave propagation in acoustic tubes of variable cross section. *The Journal of the Acoustical Society of America*, 140(1):728–740, 2016.
- [9] Stefan Bilbao, Reginald Harrison, Jean Kergomard, Bruno Lombard, and Christophe Vergez. Passive models of viscothermal wave propagation in acoustic tubes. *The Journal of the Acoustical Society of America*, 138(2):555–558, 2015.
- [10] Juliette Chabassier and Sebastien Imperiale. Space/time convergence analysis of a class of conservative schemes for linear wave equations. *Comptes Rendus Mathématique*, 355(3):282–289, 2017.

- [11] Juliette Chabassier and Robin Tournemenne. Simulation de l'impédance d'entrée de cuivres par éléments finis à une dimension. Comparaison avec les matrices de transfert. In *CFA 2018 - 14ème Congrès Français d'Acoustique*, Le Havre, France, April 2018.
- [12] Antoine Chaigne and Jean Kergomard. *Acoustics of musical instruments*. Springer.
- [13] Jer Ming Chen, John Smith, and Joe Wolfe. Experienced saxophonists learn to tune their vocal tracts. *Science*, 319(5864):776–776, 2008.
- [14] David C Copley and William J Strong. A stroboscopic study of lip vibrations in a trombone. *The Journal of the Acoustical Society of America*, 99(2):1219–1226, 1996.
- [15] JS Cullen, Joël Gilbert, and DM Campbell. Brass instruments: linear stability analysis and experiments with an artificial mouth. *Acta Acustica united with Acustica*, 86(4):704–724, 2000.
- [16] J-P Dalmont, Cornelis J Nederveen, and Nicolas Joly. Radiation impedance of tubes with different flanges: numerical and experimental investigations. *Journal of sound and vibration*, 244(3):505–534, 2001.
- [17] Patricio de la Cuadra, Benoît Fabre, Nicolas Montgermont, and Christopher Chafe. Analysis of flute control parameters: A comparison between a novice and an experienced flautist. *Acta Acustica united with Acustica*, 94(5):740–749, 2008.
- [18] Victorita Dolean, Hassan Fahs, Loula Fezoui, and Stéphane Lanteri. Locally implicit discontinuous galerkin method for time domain electromagnetics. *Journal of Computational Physics*, 229(2):512–526, 2010.
- [19] Fumiaki Ehara, Keinosuke Nagai, and Koichi Mizutani. Relationships between vibration of artificial lips and sound frequency of a trumpet. In *Proc. International Symposium on Musical Acoustics, Perugia, Italy*, pages 513–516, 2001.
- [20] Joël Gilbert, Laurent Simon, and Jonathan Terroir. Vibrato of saxophones. *The Journal of the Acoustical Society of America*, 118(4):2649–2655, 2005.
- [21] Timo Grothe and Malte Kob. High resolution 3d radiation measurements on the bassoon. 2019.
- [22] Ph Guillemain, Ch Vergez, Didier Ferrand, and Arnaud Farcy. An instrumented saxophone mouthpiece and its use to understand how an experienced musician plays. *Acta Acustica united with Acustica*, 96(4):622–634, 2010.
- [23] Philippe Guillemain, Jean Kergomard, and Thierry Voinier. Real-time synthesis of clarinet-like instruments using digital impedance models. *The Journal of the Acoustical Society of America*, 118(1):483–494, 2005.

- [24] Houssem Haddar, Thomas Hélie, and Denis Matignon. A webster-lokshin model for waves with viscothermal losses and impedance boundary conditions: strong solutions. In *Mathematical and Numerical Aspects of Wave Propagation WAVES 2003*, pages 66–71. Springer, 2003.
- [25] Houssem Haddar, J-R Li, and Denis Matignon. Efficient solution of a wave equation with fractional-order dissipative terms. *Journal of Computational and Applied Mathematics*, 234(6):2003–2010, 2010.
- [26] Ernst Hairer, Christian Lubich, and Gerhard Wanner. *Geometric numerical integration: structure-preserving algorithms for ordinary differential equations*, volume 31. Springer Science & Business Media, 2006.
- [27] Th Hélie and Denis Matignon. Diffusive representations for the analysis and simulation of flared acoustic pipes with visco-thermal losses. *Mathematical Models and Methods in Applied Sciences*, 16(04):503–536, 2006.
- [28] Thomas Hélie, Thomas Hézard, Rémi Mignot, and Denis Matignon. On the 1D wave propagation in wind instruments with a smooth profile. In *Forum Acusticum*, pages 1–6, Aalborg, Denmark, July 2011. cote interne IRCAM: Helie11d.
- [29] Thomas Hélie and Xavier Rodet. Radiation of a pulsating portion of a sphere: Application to horn radiation. *Acta Acustica united with Acustica*, 89(4):565–577, 2003.
- [30] Hermann Helmholtz. *On the Sensations of Tone, trans. AJ Ellis*. New York: Dover Publications, Inc.[Original work published in 1877], 1877.
- [31] Tohru Idogawa, Tokihiko Kobata, Kouji Komuro, and Masakazu Iwaki. Nonlinear vibrations in the air column of a clarinet artificially blown. *The Journal of the Acoustical Society of America*, 93(1):540–551, 1993.
- [32] Elodie Joliveau, John Smith, and Joe Wolfe. Acoustics: tuning of vocal tract resonance by sopranos. *Nature*, 427(6970):116, 2004.
- [33] Patrick Joly. *Analyse et approximation de modèles de propagation d’ondes. Analyse mathématique*. École Polytechnique, 2001.
- [34] Wilfried Kausel. Optimization of brasswind instruments and its application in bore reconstruction. *Journal of New Music Research*, 30(1):69–82, 2001.
- [35] Jean Kergomard. Elementary considerations on reed-instrument oscillations. *Mechanics of musical instruments*, pages 229–290, 1995.
- [36] Gustav Kirchhoff. Ueber den einfluss der wärmeleitung in einem gase auf die schallbewegung. *Annalen der Physik*, 210(6):177–193, 1868.
- [37] Roberta L Klatzky, Dinesh K Pai, and Eric P Krotkov. Perception of material from contact sounds. *Presence: Teleoperators & Virtual Environments*, 9(4):399–410, 2000.
- [38] Daniel W Martin. Directivity and the acoustic spectra of brass wind instruments. *The Journal of the Acoustical Society of America*, 13(3):309–313, 1942.

- [39] Jürgen Meyer. Akustik und musikalische aufführungspraxis: Fachbuchreihe das musikinstrument. 1972.
- [40] Rémi Mignot, Thomas Hélie, and Denis Matignon. Digital waveguide modeling for wind instruments: Building a state-space representation based on the webster-lokshin model. *IEEE transactions on audio, speech, and language processing*, 18(4):843–854, 2010.
- [41] Mamadou N’diaye. *On the study and development of high-order time integration schemes for odes applied to acoustic and electromagnetic wave propagation problems*. Theses, Université de Pau et des pays de l’Adour, December 2017.
- [42] Ricardo H Nochetto, Kunibert G Siebert, and Andreas Veerer. Theory of adaptive finite element methods: an introduction. In *Multiscale, nonlinear and adaptive approximation*, pages 409–542. Springer, 2009.
- [43] Yasuo Obikane. Direct simulation on a fipple flute using the compressible navier–stokes equation. *World Acad. Sci. Eng. Technol*, 4:794–798, 2009.
- [44] Alfio Quarteroni, Riccardo Sacco, and Fausto Saleri. *Méthodes Numériques: Algorithmes, analyse et applications*. Springer Science & Business Media, 2008.
- [45] Sjoerd Rienstra. The webster equation revisited. In *8th AIAA/CEAS Aeroacoustics Conference & Exhibit*, page 2520.
- [46] Sebastian Schmutzhard, Vasileios Chatziioannou, and Alex Hofmann. Parameter optimisation of a viscothermal time-domain model for wind instruments.
- [47] Y Shi, A Da Silva, and G Scavone. Numerical simulation of whistles using lattice boltzmann methods.
- [48] Taka’aki Tachibana and Kin’ya Takahashi. Sounding mechanism of a cylindrical pipe fitted with a clarinet mouthpiece. *Progress of Theoretical Physics*, 104(2):265–288, 2000.
- [49] Alex Tarnopolsky, Neville Fletcher, Lloyd Hollenberg, Benjamin Lange, John Smith, and Joe Wolfe. Acoustics: the vocal tract and the sound of a didgeridoo. *Nature*, 436(7047):39, 2005.
- [50] Robin Tournemenne, Bastien Talgorn, Jean-François Petiot, Joel Gilbert, and Michael Kokkolaras. Optimization of brass wind instruments based on sound simulations. 2018.